COMPUTATIONAL MODELLING OF HEAT TRANSFER IN AN ANNULAR POROUS MEDIUM SOLAR ENERGY ABSORBER WITH THE P1-RADIATIVE DIFFERENTIAL APPROXIMATION

O. Anwar Bég [1] *, Nasir Ali[2], Akbar Zaman[2], Eemaan T. A. Bég[3] and Ayesha Sohail[4]

[1]*Fluid Mechanics, Spray Research Group, Petroleum and Gas Engineering Division, School of Computing, Science and Engineering, Newton Building, University of Salford, Manchester, M54WT, **UK***
[2]*Department of Mathematics and Statistics, International Islamic University, Islamabad, 44000, **Pakistan**.*
[3]*Multi-Physics Simulations, Israfil House, Dickenson Rd, Manchester, M13, **UK**.*
[4]*Dept. Mathematics, COMSATS Institute of Information Technology, Lahore 54000, **Pakistan**.*
* Corresponding Author; - email: O.A.Beg@salford.ac.uk; gortoab@gmail.com; Tel+44 01612954570

Summary

We study the steady, laminar thermal convection flow in a participating, absorbing-emitting fluid-saturated porous medium occupying a cylindrical annulus with significant thermal radiation effects as a simulation of a solar energy absorber system. The dimensionless incompressible, viscous conservation equations for mass, axial momentum, radial momentum, heat conservation and radiative transfer equation are presented with appropriate boundary conditions in an axisymmetric (X, R) coordinate system. The Traugott P1-Differential radiative transfer model is used which reduces the general integro-differential equation for radiation heat transfer to a partial differential equation. The Darcy-Forcheimmer isotropic porous medium drag force model is employed to simulate resistance effects of the solar porous medium with constant permeability in both the radial (R) and axial (X) direction. A numerical finite difference (FTCS) scheme is used to compute the velocity (U,V), temperature (Θ) and dimensionless zero moment of intensity (I₀) distributions for the effects of conduction-radiation parameter (N), Darcy parameter (Da), Forchheimer parameter (Fs), Rayleigh buoyancy number (Ra), aspect ratio (A) and Prandtl number (Pr). The computations have shown that increasing aspect ratio increases both axial and radial velocities and elevates the radiative moment of intensity. Increasing Darcy number accelerates both axial and radial flow whereas increasing Forchheimer number decelerates the axial and radial flow. Higher values of optical thickness induce a weak deceleration in the radial flow whereas they increase both axial flow velocity and temperature. Increasing optical thickness also reduces radial radiative moment of intensity at intermediate axial coordinate values but enhances them at low and high axial coordinate values. Extensive validation is conducted with the network thermo-electric simulation program RAD-SPICE. The model finds important applications in solar energy porous wafer absorber systems, crystal growth technologies and also chemical engineering thermal technologies.

Key words: *Radiative; Convection; FTCS; RAD-SPICE; Solar energy; Rayleigh number.*

Nomenclature

Roman

a	Darcy parameter in Darcy-Forchheimer drag force model $(= \mu/K)$
A	aspect ratio
b	Forchheimer form drag (second order) parameter in Darcy-Forchheimer drag force model
D	annular gap radius $(= r_o\text{-}r_i)$
Da	Darcy number (dimensionless permeability parameter)
Fs	Forchheimer inertial number
G	incident radiation
H	height of cylindrical annulus
g	acceleration due to gravity
I_o	dimensionless zero moment of intensity
i_o	zero moment of radiation intensity
K	permeability of saturated porous medium
k	thermal conductivity of saturated porous medium
N	conduction: radiation heat transfer parameter
Nu	local Nusselt number
$\tilde{N}u$	mean Nusselt number
$N+1$	number of uniformly discretized axial points X_i (i=1,2,…N+1) in FTCS method
p	pressure
p_∞	reference pressure
P	dimensionless pressure
∇p	pressure gradient in Darcy-Forchheimer drag force model
$\dfrac{\partial P}{\partial X}$	axial pressure gradient
$\dfrac{\partial P}{\partial R}$	radial pressure gradient
Pr	Prandtl number
q_ξ^r	ξ-direction radiative heat transfer flux
q_η^r	η-direction radiative heat transfer flux
r	dimensional radial coordinate
r_i	inner cylinder radius
r_o	outer cylinder radius
$r*$	radius ratio
R	dimensionless radial coordinate
Ra	Rayleigh free convection (buoyancy) number
R_k	number of radial points $=(k\text{-}1)\,\Delta R$ $(k=1,2,…)$ in FTCS difference method
ΔR	radial grid spacing in FTCS difference method
T_h	constant Inner cylinder wall temperature
T_c	constant outer cylinder wall temperature
u	dimensional axial velocity
U	dimensionless axial velocity
U_k^i	value of U at axial node X_i and at radial node R_k
v	dimensional radial velocity
V	dimensionless radial velocity
x	dimensional axial coordinate
X	dimensionless axial coordinate
ΔX	axial grid spacing $(=1/(N+1))$ in FTCS difference method

Greek

α	thermal diffusivity of the gray fluid
β	coefficient of thermal expansion
μ	dynamic viscosity of the gray fluid in porous medium
ρ	density of the gray fluid
ϕ	temperature function
τ_0	optical thickness of the saturated porous medium
σ	Stefan-Boltzmann constant,
σ_a	absorption coefficient
ω	albedo
ψ	general velocity in Darcy-Forchheimer drag force model
Θ	dimensionless temperature function
Θ_f	dimensionless reference temperature ratio
χ	modified viscosity parameter
λ	modified thermal diffusivity parameter
ν	kinematic viscosity of gray fluid

1. INTRODUCTION

Numerical modeling of heat transfer processes in energy systems and technologies has developed considerably in the last two decades. This approach provides a relatively inexpensive and powerful compliment to experimental and field-based testing of energy devices. Numerous techniques have been developed to provide faster and more accurate simulations of complex, multi-physical transport processes arising in solar power cells [1], hybrid batteries [2], magnetohydrodynamic (MHD) pumps [3], electrohydrodynamic (EHD) pumps [4] and other renewable energy systems [5]. Both academic and commercial industrial research in energy systems, which is fundamental to mechanical, chemical, biomedical and materials processing systems, has benefited immensely from the many different computational solvers which have been developed, refined and implemented. These include finite element methods [6], alternating direction implicit (ADI) finite difference techniques [7], spectral collocation solvers [8], smoothed particle hydrodynamics (SPH) which is an alternative mesh-free Lagrangian method [9], neural network and genetic algorithms [10], CFD softwares e.g. FLUENT [11], network

simulation codes [12] and control volume computational solvers [13]. *Solar energy engineering* presents a particularly rich forum for the implementation of advanced numerical analysis since the phenomena encapsulated in realistic solar energy simulations involve phase change, surface effects, gel systems, transient heat transfer, complex geometries, the fluid dynamics of enclosures and of course thermal radiation heat transfer. The urgency for green alternatives to current methods also provides a great stimulus for expanding research in solar power. Thermal radiation heat transfer is a particularly challenging component of solar energy systems modeling since owing to coupling with other heat transfer modes, the resulting interaction of conduction, convection and radiative heat transfer generates highly nonlinear partial differential equation systems. The principal difficulty posed by radiative transfer problems is the complexity of the general equation for radiation which is of the *integro-differential type*, as described by Hottell and Sarofim [14]. Even in one-dimensional radiative heat transfer with simple geometries this equation can be challenging to solve accurately. Approximation methods are therefore employed to simulate radiative effects, in particular where thermal radiation is coupled with thermal convection. Examples of these algebraic "flux" approximations include Rosseland's diffusion approximation, Schuster-Schwartzchild two-flux approximation, Jeans P-N (spherical harmonics) approximation, the Milne-Eddington differential approximation and most complex of all, the Chandrasekhar discrete ordinates (*S-N*) approximation [14]. Several excellent studies have considered thermal radiation effects in solar energy heat transfer. Siebers and Viskanta [15] used a dual spectral band model to simulate the coupled conductive-convective-radiative heat transfer from the absorber of a flat plate solar collector analytically. They showed that a single selective surface on the absorber provides the best performance in terms of minimized radiation heat transfer losses. Bohn and Mehos

[16] employed two-flux, discrete ordinate, and the Monte Carlo methods for radiative transport simulation of the radiative intensity field and absorbed solar flux effects in the behavior of solar-driven chemical reactors for the case of an axisymmetric cylinder with a specified intensity field at one end, diffuse reflection at boundaries, and containing a participating medium. Chow and Chan [17] studied solar radiation effects in solar-collector orientations for the coastal region of South China, showing that a solar collector facing the south-west direction could be most desirable for a wide range of tilt angles, and for maximizing the annual yield. Leutz and Annen [18] used a reverse ray-tracing method together with a solar radiation heat transfer model to study the annual energy collection efficiency of stationary and quasi-stationary (seasonally tilted) solar concentrators. Augustus and Kumar [19] studied parametrically the effects of porosity, airflow rate, solar radiation, and solar absorptivity/thermal emissivity on collector efficiency, heat exchange effectiveness, air temperature rise and useful heat delivered in unglazed transpired solar collectors.

In the above studies generally only *pure fluid regimes* were considered. However the presence of a porous medium has been shown to have a positive influence in the design of solar energy absorbers [20]. Generally for low velocity transport in porous systems the Darcian model [21] is implemented. Such a model is only valid when the Reynolds number based on the pore size is less than unity i.e. "creeping" flows. For higher velocity flows however, beyond a Reynolds number of 10, and in porous media of large pore radius, the Darcy model is no longer sufficient to accurately simulate porous media hydrodynamic effects since it neglects inertial drag forces and also boundary vorticity diffusion (Brinkman friction) effects which become significant at higher velocities and near enclosing boundaries, respectively. Kleinstreuer and Chiang [22] studied numerically the porous-

medium flat-plate solar collector as an alternative to conventional fin-and-tube designs using a non-Darcy flow equation and convection-conduction heat transfer equation, showing that the porous medium results in high-performance efficiency compared with advanced tubular-type collectors. Bég *et al*. [23] studied the dissipative thermal convection flow in Darcy-Brinkman porous media using a numerical difference scheme for a wide range of Eckert numbers. Rabadi and Mismar [24] designed two solar energy collectors employing curved channel technology and porous media (with a porosity of 0.1453) aimed at enhancing heat transfer performance and for extra energy storage capability. The porous medium was shown to strongly reduce the rate of decline in water temperature to approximately half its value for the non-porous medium case. Other studies of thermal convection in porous media with applications in solar energy absorber modeling and other topics have been discussed at length by Nield and Bejan [25]. Several studies have examined thermal radiation effects on convection in Darcy-Forchheimer porous media. Takhar *et al* [26] used the Keller-Box implicit difference solver to simulate combined radiation-convection flow in non-Darcy porous media with the Cogley-Vinceti-Giles differential radative equilibrium approximation and viscous dissipation effects. Nagaraju *et al*. [27] studied the composite radiative-convective heat transfer in a variable-porosity medium using the Schuster-Schwatrzchild two-flux radiation approximation. Bég and Takhar [28] obtained numerical solutions for heat transfer in second order viscoelastic fluid from a wedge embedded in Darcy-Forchheimer-Brinkman porous media with the Rosseland radiation model. Bég *et al.* [29] investigated the mixed radiation-convection flow of an optically dense viscous fluid in a non-Darcy porous medium using a diffusion approximation. Transient radiation-convection flow in porous media have also been studied for the *Darcian* case and *non-Darcian* case, respectively by Bég *et al.* [30, 31]

using Network Simulation Methodology (NSM). A more complex thermal radiation model, the *P1 spherical harmonics model* however has been shown by Bouallou and Sacadura [32] to more accurately predict radiative heat transfer in the optically-thick limit in enclosures, compared with the Schuster flux model or the Rosseland model. In the present article we therefore study theoretically and computationally the combined thermal convection and radiative heat transfer flow of an absorbing, emitting and non-scattering gray fluid in a cylindrical porous annulus system containing a Darcy-Forchheimer porous medium using a numerical method. The *P-1 radiative approximation* is employed and requires numerical solution of a supplementary radiative heat transfer partial differential equation, in addition to the energy conservation and momentum conservation equations. We study the influence of radiation-conduction parameter, Rayleigh number, optical thickness, Darcy number, Forcheimmer number and aspect ratio on the velocity, radiative moment of intensity and temperature field distributions in the annular regime. The study is relevant to hybrid porous media solar cell collectors.

2. MATHEMATICAL THERMAL CONVECTION-RADIATION MODEL

We study the hydrodynamics and heat transfer of an incompressible, absorbing, emitting and non-scattering, gray, Newtonian fluid in an anisotropic, non-Darcian, porous medium filling a vertical cylindrical annulus enclosure possessing "black" walls. The physical regime is depicted below in **figure 1**. The upper and lower surfaces of the enclosure are adiabatic. The *P1-radiative transfer model* is adopted from the Traugott analysis [33]. Bayazitoglu and Higenyi [34] have indicated that the P1 model provides accuracy of about 90% for *optical thicknesses up to unity.* It is therefore a *superior radiative model* to, for example, the popular Rosseland diffusion flux model [35, 36]. The P1-model for two-

dimensional systems with general coordinates (ξ, η) may be expressed as follows, following Weng and Chu [37]:

$$\frac{\partial^2 G}{\partial \xi^2} + \frac{\partial^2 G}{\partial \eta^2} - 3\tau_0^2 (1-\omega)G = -12\tau_0^2 (1-\omega)\phi^4 \tag{1}$$

$$q_\xi^r = \frac{1}{3\tau_0} \frac{\partial G}{\partial \xi} \tag{2}$$

$$q_\eta^r = \frac{1}{3\tau_0} \frac{\partial G}{\partial \eta} \tag{3}$$

where q_ξ^r is the ξ-direction radiative heat transfer flux, q_η^r is the η-direction radiative heat transfer flux, G denotes the incident radiation, τ_0 is the optical thickness of the medium, ω is the albedo and ϕ is a temperature function. The gradients of the functions in (2) and (3) are therefore introduced into the energy conservation equation in the present problem. For two-dimensional axisymmetric porous *isotropic* flow, in an (X,R) i.e. axial-radial coordinate system, we shall utilize a single permeability (K) in the axial and radial directions to simulate porous media hydraulic conductivity. We implement the *Darcy–Forchheimer model* which is a second order relationship defining the pressure gradient as:

$$\nabla p = -a\Psi + b\Psi^2 \tag{4}$$

where ψ denotes a general velocity, ∇p is pressure gradient, a and b are constants defined by $a = \mu/K$ and b is a function of the geometry of porous medium i.e. b is the Forcheimmer form-drag parameter for quadratic effects and μ is the dynamic viscosity of the gray fluid. The flow regime is illustrated in figure 1 below. The inner cylinder has a radius r_i and is maintained at isothermal conditions (temperature T_h); the outer cylinder has radius r_o and

is also at constant temperature, T_c. The X-coordinate is directed along the vertical axis parallel to the height dimension of the system and the radial coordinate is normal to this. The regime is one of buoyancy and simulated via the Boussinesq approximation. When the radiative flux equations (2) and (3) are included in the generalized Navier-Stokes equations in an *axisymmetric* coordinate system, neglecting tangential momentum contributions, the dimensionless conservation equations can be shown to take the form:

Mass Conservation

$$\frac{\partial(RU)}{\partial X} + \frac{\partial(RV)}{\partial R} = 0 \tag{5}$$

Axial (X-direction) Momentum Conservation

$$\frac{1}{R}[\frac{\partial(RUU)}{\partial X} + \frac{\partial(RVU)}{\partial R}] = -\frac{\partial P}{\partial X} + \frac{\Pr}{R}[\frac{\partial}{\partial X}(R\frac{\partial U}{\partial X}) + \frac{\partial}{\partial R}(R\frac{\partial U}{\partial R})]$$
$$+ Ra\Pr\Theta - \frac{1}{Da}\chi U - \frac{Fs}{Da}\lambda U^2 \tag{6}$$

Radial (R-direction) Momentum Conservation

$$\frac{1}{R}[\frac{\partial(RUV)}{\partial X} + \frac{\partial(RVV)}{\partial R}] = -\frac{\partial P}{\partial R} + \frac{\Pr}{R}[\frac{\partial}{\partial X}(R\frac{\partial V}{\partial X}) + \frac{\partial}{\partial R}(R\frac{\partial V}{\partial R})]$$
$$- \Pr\frac{V}{R^2} - \frac{1}{Da}\chi V - \frac{Fs}{Da}\lambda V^2 \tag{7}$$

Energy (Heat) Conservation

$$\frac{1}{R}[\frac{\partial(RU\Theta)}{\partial X} + \frac{\partial(RV\Theta)}{\partial R}] = \frac{1}{R}[\frac{\partial}{\partial X}(R\frac{\partial\Theta}{\partial X}) + \frac{\partial}{\partial R}(R\frac{\partial\Theta}{\partial R})] + \frac{\Theta_f\tau_0^2}{N}[(\frac{\Theta}{\Theta_f}+1)^4 - I_0] \tag{8}$$

Radiative Transfer Equation

$$\frac{1}{R}[\frac{\partial}{\partial X}(R\frac{\partial I_0}{\partial X}) + \frac{\partial}{\partial R}(R\frac{\partial I_0}{\partial R})] = 3\tau_0^2[I_0 - (\frac{\Theta}{\Theta_f}+1)^4] \tag{9}$$

where $X = \dfrac{x}{D}$ and $R = \dfrac{r}{D}$ are dimensionless axial and radial coordinates, $U = \dfrac{uD}{\alpha}$ and

$V = \dfrac{vD}{\alpha}$ are dimensionless axial and radial velocity components in the X and R directions,

$P = \dfrac{p - p_\infty}{\rho(\alpha / D)^2}$ is dimensionless pressure, α is thermal diffusivity of the gray fluid, ρ is

density of the gray fluid, $\Theta = \dfrac{T - T_c}{T_h - T_c}$ is dimensionless temperature function,

$\Theta_f = \dfrac{T_c}{T_h - T_c}$ is dimensionless reference temperature ratio, $N = \dfrac{k\sigma_a}{4\sigma T_c^3}$ is the *conduction:*

radiation heat transfer parameter, $I_o = \dfrac{i_o}{4\sigma T_c^4}$ is the dimensionless zero moment of

intensity in which i_o is zero moment of radiation intensity, σ is the Stefan-Boltzmann

constant, $\tau_0 = \sigma_a D$ is optical thickness where σ_a is the absorption coefficient, $A = \dfrac{H}{D}$ is

the aspect ratio, $r^* = \dfrac{r_i}{r_o}$ is the radius ratio, $D = r_o\text{-}r_i$ is annular gap radius, $\mathrm{Pr} = \dfrac{v}{\alpha}$ is the

Prandtl number, $Ra = \dfrac{g\beta(T_h - T_c)D^3}{v\alpha}$ is the Rayleigh free convection (buoyancy) number,

$Da = \dfrac{K}{D^2}$ is the Darcy number (dimensionless permeability parameter) for both radial and

axial directions, $Fs = \dfrac{b}{L}$ is the Forchheimer inertial number for both radial and axial

directions, χ is a modified viscosity parameter, λ is a modified thermal diffusivity

parameter, ρ is density of gray fluid, β is coefficient of thermal expansion, v is kinematic

viscosity of gray fluid, σ is the Stefan-Boltzmann constant, k is thermal conductivity, g is

acceleration due to gravity. In equation (6) $+Ra\,\mathrm{Pr}\,\Theta$ is the *buoyancy* (free convection) term, coupling the axial momentum equation (6) to the energy equation (8). Also in Eqn. (6) the penultimate term on the right hand side is the *axial Darcian drag force* and the last term is the *axial Forchheimer drag force*. Similarly in equation (7) the penultimate term is the *radial Darcian impedance* and the final term on the right hand side is the *radial Forchheimer impedance*. The corresponding boundary conditions are as follows:

At $R=\ 1/(r^*-1)$: $\qquad U = V = 0,\ \Theta = 1,\ \ (1-\dfrac{2}{3\tau_0}\dfrac{\partial}{\partial R})I_0 = [\dfrac{1}{\Theta_f}+1]^4$ $\qquad\qquad$ (10)

At $R=\ r^*/(r^*-1)$: $\qquad U = V = 0,\ \Theta = 0,\ \ (1+\dfrac{2}{3\tau_0}\dfrac{\partial}{\partial R})I_0 = 1$ $\qquad\qquad$ (11)

At $X=\ 0$: $\qquad U = V = 0,\ \dfrac{\partial\Theta}{\partial X}+\dfrac{1}{3N}\dfrac{\partial I_0}{\partial X}=0,\qquad (1-\dfrac{2}{3\tau_0}\dfrac{\partial}{\partial X})I_0 = [\dfrac{\Theta}{\Theta_f}+1]^4$ $\quad$ (12)

At $X=\ A$: $\qquad U = V = 0,\ \dfrac{\partial\Theta}{\partial X}+\dfrac{1}{3N}\dfrac{\partial I_0}{\partial X}=0,\qquad (1+\dfrac{2}{3\tau_0}\dfrac{\partial}{\partial X})I_0 = [\dfrac{\Theta}{\Theta_f}+1]^4$ $\quad$ (13)

In practical solar engineering design, the boundary heat transfer rates for the annulus are important. We may therefore define the local Nusselt number on the inner vertical cylinder and the outer vertical cylinder, which take the form:

$$Nu = -R(\dfrac{\partial\Theta}{\partial R}+\dfrac{1}{3N}\dfrac{\partial I_0}{\partial R}) \qquad\qquad\qquad (14)$$

where the appropriate value for the radius is used for the two cases. Additionally a *mean Nusselt number* may be computed by integrating the local Nusselt number along the cylindrical wall surface, viz:

$$\tilde{Nu} = \frac{1}{A} \int_0^A Nu \ dX \qquad (15)$$

A number of special cases can be derived from the transformed momentum, energy and radiative transfer equation (5) to (9). As *Fs* → *0*, inertial porous hydromechanical drag effects vanish and the regime becomes a purely Darcian (isotropic) porous medium. With *Da* → ∞ and *Fs* → *0*, all porous hydrodynamical body forces vanish. This implies that the porous matrix permeability becomes infinite so that the regime is purely fluid in the annulus. Equations (6) and (7) are therefore reduced to the model solved by Weng and Chu [37] with the same boundary conditions, although their study infact ignores variation of Prandtl number. As *Ra* → *0*, buoyancy forces vanish and only the *X-direction (axial) momentum equation* (6) is affected. With *N* → ∞, radiative heat transfer effects are negated and this affects the energy conservation equation (8); the radiative transfer equation (9) also vanishes.

3. FTCS NUMERICAL SIMULATION

Numerical solutions to the governing transformed partial differential equations (5) to (11) under boundary conditions (12) to (15) are to be obtained using a robust finite difference numerical method. We utilize a well-tested, versatile, explicit numerical scheme which is *forward in time* and *central in space* [38]. This scheme has been successfully applied to a variety of complex geometric and material non-linear fluid dynamics problems [39-41].

According to this scheme the various axial and radial partial derivatives of U, V, Θ, I_O appearing in (5)-(9) are approximated as, for example:

$$\frac{\partial U}{\partial X} \cong \frac{U_{i+1}^{k} - U_{i-1}^{k}}{2\Delta X} = U_X \tag{16}$$

$$\frac{\partial^2 U}{\partial X^2} \cong \frac{U_{i+1}^{k} - 2U_{i}^{k} + U_{i-1}^{k}}{(\Delta X)^2} = U_{XX} \tag{17}$$

$$\frac{\partial U}{\partial R} \cong \frac{U_{i+1}^{k} - U_{i-1}^{k}}{2\Delta R} = U_R \tag{18}$$

$$\frac{\partial \Theta}{\partial R} \cong \frac{\Theta_{i+1}^{k} - \Theta_{i-1}^{k}}{2\Delta R} = \Theta_R \tag{19}$$

$$\frac{\partial I_O}{\partial R} \cong \frac{I_{O i+1}^{k} - I_{O i-1}^{k}}{2\Delta R} = I_{OR} \tag{20}$$

where for instance, U_k^i denotes the value of U at axial node X_i and at radial node R_k. Similar expressions for other partial derivatives may then be derived. With the aid of Eqns. (5)-(9), the numerical solution can be generated for $(N+1)$ uniformly discretized points X_i $(i=1,2,...N+1)$, with an axial grid spacing of $\Delta X=1/(N+1)$, and at radial points $R_k =(k-1)$ ΔR $(k=1,2,...)$, with a radial grid spacing of ΔR. Test computations are performed for the present case. A stable solution with an accuracy of 10^{-7} is achievable.

4. VALIDATION WITH NETWORK SIMULATION METHOD (NSM)

To verify the accuracy of the **FTCS** computations, we have also solved the nonlinear boundary value problem with a modified version of the electro-thermal solver, PSPICE [42], namely **RAD-PSPICE**. The transformed partial differential equations (8) to (10) subject to the temporal and spatial boundary conditions (11) have been solved with the **RAD-PSPICE N**etwork **S**imulation **M**ethod software (**NSM**) approach in a **MATLAB** environment. This technique is founded on the *thermo-electrical analogy* and has been implemented in many diverse areas of applied mechanics, thermal sciences and fluid dynamics, being equally adept at solving linear and non-linear, steady or transient, hydrodynamic or coupled transport problems. Network simulation methodology uses the *network theory of thermodynamics*, in which flux-force relationships in dynamical systems are modelled using electric networks. NSM effectively exploits the formal similarities between the mathematical structure underlying different phenomena with the same balance and constitutive equations and intrinsic to this approach is the design of an "analogous electric circuit" which possesses the same balance and constitutive equations as the physical problem of interest. **NSM** was introduced by Nagel [42] originally for semi-conductor and transient electrical circuit problems. It has also been implemented in magnetic tribology (squeeze films for spacecraft landing gear) [43], magnetic biopolymer materials processing [44], magneto/electro-rheological (M/ER) smart lubrication systems for earthquake shock protection (seismic bearings) [45], electro-kinetic stabilization of geotechnical materials [46], stratified materials processing flows [47] and rotating Couette flows [48]. Discretization of the *differential* equations is founded on the *finite-difference methodology*, where only a discretization of the spatial co-ordinates is necessary. Numerical differentiation is implicit in such methods and some expertise is

required in avoiding numerical diffusion, instability and convergence problems. **NSM** simulates the *electrical variable of voltage* as being equivalent to the velocities (U, V), temperature (Θ) and dimensionless zero moment of radiation intensity (I_o), while the *electrical current* is equivalent to the velocity flux e.g. *($\partial U/\partial X$, $\partial V/\partial R$)*, temperature flux e.g. ($\partial \Theta/\partial X$, $\partial \Theta/\partial R$) and radiation intensity flux e.g. ($\partial I_o/\partial X$, $\partial I_o/\partial R$)). A network electrical model for *each* volume element is designed so that its electrical equations are formally equivalent to the spatial discretized equation. The whole network model, including the devices associated with the boundary conditions, is solved by the modified numerical computer code **Pspice** [49]. *Fourier's* law is utilized in the spatial discretization of the dimensionless transport equations. The electrical analogy is applied to the discretized equations together with *Kirchhoff´s law* for electrical currents. To implement the boundary conditions, constant voltage sources are employed for velocity, temperature and concentration. *Time* remains as a real continuous variable. Researchers need not manipulate the finite difference differential equations to be solved nor expend effort in convergence exercises. The principal advantage of NSM is that it negates the requirement in standard numerical finite difference schemes of manipulation of difference equations and the constraints of specified yardsticks around the convergence of numerical solutions. Details of the discretization and electronic network diagram construction have been provided in many previous studies and the reader is referred to Bég *et al*. [49]. The MAG-PSPICE code is designated the "electric circuit simulator". Nagel [42] has elucidated in detail the local truncation errors present in the original **SPICE** algorithm. A necessary criterion for using **RAD-SPICE** effectively is a familiarity with electrical circuit theory. Momentum, temperature and concentration balance "currents" are defined systematically for each of the discretized equations and

errors can be quantified in terms of the quantity of control volumes. The user however needs to program a customized protocol file, (file "*RadNetwork.cir*"). This program rapidly generates the file for execution in RAD-PSPICE, and the program permits the reading of the solutions provided by RAD-PSPICE (file "*RadNetwork.out*"). Following the simulations, the code plots waveform results so the designer can visualize circuit behavior and determine design validity. Graphical results of each simulation are presented in the RAD-PSPICE "Probe window waveform viewer" and analyzer, where it is possible to see the velocity, temperature and concentration field at any point of the boundary layer. A summary of the procedure is given in **Fig. 2** below. **NSM** implements the most recent advances in software in the resolution of electrical networks to solve diverse types of partial differential equations which may be *elliptical, hyperbolical, parabolic, linear, non-linear* and *1-, 2- or 3-dimensional*. At least one of the FTCS finite difference computations in each validated graph has been closely verified with RAD-PSPICE. The NSM (RAD-PSPICE) solutions are given the   symbol in selected graphs (**Figs. 3-10**) presented. The FTCS computations are therefore shown to be highly accurate as corroborated by an independent numerical simulation tool. Although simpler models do exist with which we can benchmark very special reduced cases of the general model presented in the current article, we have opted to validate the *general model* including all hydrodynamic and heat transfer effects. This is a significantly more zealous approach and confirms general solutions obtained by the FTCS code with the RAD-SPICE code. Moreover, it provides extensive confidence to other researchers who may wish to extend the present model to for example *non-Newtonian* flow and are therefore provided with solutions to validate their own programs.

5. NUMERICAL RESULTS AND DISCUSSION

In the present study we present an extensive range of FTCS solutions. **Figs 3-10** include

RAD-SPICE validation. The nonlinear boundary value problem entails 4 variables to

compute in the axial (*X*) and radial (*R*) direction i.e. *U, V, Θ, I_o*. The regime conservation

equations and boundary conditions are controlled by 9 thermo-physical parameters: *Pr, Ra,*

Da, Fs, λ, χ, τ_0, Θ_f, N and 2 geometric parameters i.e. *A* and r_i. We note that $A = \dfrac{H}{D}$ i.e.

aspect ratio, represents the ratio of height of the cylinders to the gap radius, *H* height

of cylindrical annulus, *D (= r_o-r_i)* and $r* = \dfrac{r_i}{r_o}$ is the radius ratio and generally for an

annular regime $r_o > r_i$. For example for $r_o = 2r_i$, *r* = 0.5, for $r_o = 4r_i$, r* = 0.25*. We consider

the case of constant axial and radial pressure gradients, so these parameters may be

prescribed unity values i.e. In Eqn (6), $\dfrac{\partial P}{\partial X}$ = -1 and in Eqn (7), $\dfrac{\partial P}{\partial R}$ = -1. We primarily

study the effects of *Ra, Da, Fs, N, A and τ_0*. In the plots dimensionless radius, *R*, is denoted

by numerical *r*. Generally we prescribe *Pr = 2.0 (water-based suspensions), Da = 0.1 (very*

high permeability), Fs = 1 (weak quadratic porous drag) are prescribed.

Evidently in **fig. 3** an increase in Rayleigh number accelerates the axial flow. With *Ra > 1*,

the thermal buoyancy force exceeds the viscous hydrodynamic force. This aids momentum

development and increases velocities. The axial velocity profiles also evolve from a plateau

structure at lower Rayleigh numbers to a more parabolic nature at higher Rayleigh

numbers. The Rayleigh number, $Ra = \dfrac{g\beta(T_h - T_c)D^3}{\nu\alpha}$, arises only in the *axial momentum*

eqn. (6) and couples this equation to the energy eqn. (8) via the term, *Ra PrΘ*. Although

linear, this term has a profound effect on the interaction of heat transfer and momentum in

the regime. **Fig. 4** presents the temperature variation across the annular zone with variation in Rayleigh number. At low radial coordinate values, the temperature is found to be enhanced with greater R_a i.e. increasing thermal buoyancy force; however at further radial values the opposite behavior becomes apparent. The Rayleigh numbers required to achieve a change in temperature are orders of magnitude greater than for the velocity field. Momentum is therefore extremely sensitive to buoyancy effects whereas temperature field is much less responsive. Velocity vanishes at the initial and final radial coordinate values, whereas temperature has a non-zero value here in accordance with the specified boundary conditions. Temperatures at *r=0* are however in excess of those at *r= 2*, irrespective of the Rayleigh number value. **Fig. 5** illustrates the effect of Rayleigh number on d*imensionless zero moment of intensity (I₀) in the axial direction.* In the present study we have aimed to *directly address the response of this radiative heat transfer characteristic*, in addition to elucidating the effect of conduction-radiation parameter (*N*), rather than *indirectly* studying solely the influence of radiative heat transfer on velocity and thermal fields. The former direct methodology has been followed by Bouallou and Sacadura [32]. The latter indirect approach yields very limited understanding of the physics of radiative heat transfer- it is an approach that was adopted for example by Weng and Chu [37]. Evidently *I₀ magnitudes* are suppressed with *increasing Rayleigh number;* they are observed to peak at central axial coordinate values. There is very strong dual coupling between the energy (temperature) field in eqn. (8) and the radiative field i.e. eqn. (9). For example in the former we observe

the algebraic term $+\dfrac{\Theta_f {\tau_0}^2}{N}[(\dfrac{\Theta}{\Theta_f}+1)^4 - I_0]$. In this term only, $N = \dfrac{k\sigma_a}{4\sigma {T_c}^3}$ i.e. the

conduction: radiation heat transfer parameter also arises. In the latter, another algebraic

term arises, viz: $3{\tau_0}^2[I_0 - (\dfrac{\Theta}{\Theta_f}+1)^4]$. In both terms zero moment of intensity is linear

whereas in the former temperature is both linear and quartic, whereas in the latter it is a quartic term. Despite these terms, physically the Rayleigh number only exerts a very weak influence on radiative field. The dominant influence is on the velocity field owing to the buoyancy effect. **Fig. 6** shows that moment of intensity, I_o, exhibits a *montonic decay* in the *radial direction*, distinct from the *parabolic* distribution in the *axial* direction (fig. 5). Once again there is a marginal reduction in radiative moment of intensity with a very significant rise in Rayleigh number (thermal buoyancy effect).

Figs. 7-11 illustrate the influence of the permeability parameter i.e. *Darcy number* on velocity, temperature and radiative moment of intensity distributions. Radial velocity (fig. 7) is found to be strongly increased with a rise in Darcy number. *Da* appears as a denominator in the axial Darcian and Forchheimer drag force terms, $-\dfrac{1}{Da}\chi U, -\dfrac{Fs}{Da}\lambda U^2$ in eqn (6) and the radial Darcian and Forchheimer drag force terms, $-\dfrac{1}{Da}\chi V, -\dfrac{Fs}{Da}\lambda V^2$ in eqn (7). As *Da* increases the medium becomes progressively more fluid with lesser and lesser solid fibers present. This depletes both the Darcian and Forchheimer impedances, with constant χ (viscosity parameter), λ (thermal diffusivity parameter) and *Fs* (Forchheimer number). This leads to *acceleration* in the radial flow (**fig. 7**). A weak increase in temperature (**fig. 8**) also accompanies increasing Darcy number, in the axial direction. However the effect of greater Darcy number values on radial temperature distribution, albeit assistive, is very weak (**fig. 9**). Marginal elevation in radiative zero moment of intensity is also computed in both axial (**fig. 10**) and radial (**fig. 11**) directions.

Figs. 12-14 depict the evolution of axial and radial velocity components and temperature, with different Forchheimer numbers. Contrary to the Darcy number, which appears as a denominator in both Darcian and Forchheimer drag forces, as elaborated earlier,

Forchheimer number arises only as a numerator in terms, $-\dfrac{Fs}{Da}\lambda U^2$ and $-\dfrac{Fs}{Da}\lambda V^2$.

Although Forchheimer drag is second order and is related to high velocity flow, it increases as the flow velocity increases. This leads to a *substantial deceleration* in both axial (**fig. 12**) and radial (**fig. 13**) flow with increasing *Fs* values. Therefore greater *Fs* values will decrease viscous diffusion rate. This will also oppose energy diffusion. Temperatures (**fig. 14**) are therefore also reduced with greater Forchheimer effect. Higher velocity flow in the porous medium therefore acts to depress temperatures. The Forchheimer number is related more to the geometry of the porous medium and is an inertial effect, as opposed to the Darcy number which is a global representation of the medium permeability. The general trends reported in figs 12-14 concur with earlier studies by other researchers, for example Dybbs and Edwards [50]. Although we have examined *Fs* influence on radiative moment of intensity, no tangible changes were observed and therefore both axial and radial distributions are omitted here.

Fig. 15 presents the response of temperature to a variation in conduction-radiation parameter, $N = \dfrac{k\sigma_a}{4\sigma T_c^{3}}$. This parameter features as a denominator in the energy eqn. (8),

viz $\dfrac{\Theta_f \tau_0^{2}}{N}[(\dfrac{\Theta}{\Theta_f}+1)^4 - I_0]$. As *N* increase in value the radiative contribution is decreased and conductive heat transfer contribution is increased. For $N = 1$ both modes of heat transfer contribute equally. As $N\rightarrow\infty$, the radiative contribution vanishes and thermal conduction dominates. Fig. 15 shows that a significant *decrease in temperature* is induced with greater *N* values. The temperature is maximized for lowest *N* value of 0.1 i.e. strongest thermal radiation case and minimized for the largest value of $N = 1.2$ i.e. weakest thermal radiation

case. Thermal radiation therefore exerts the correct effect on temperature distributions i.e. heats the saturated porous medium by introducing significant thermal energy.

Figs 16-19 exhibit the variation in axial and radial velocity, temperature and radiative moment of intensity with a change in the annulus aspect ratio (*A*). $A = \dfrac{H}{D}$ which defines the ratio of height of the cylinders to the gap radius, *D (= r_o-r_i)*. For *A>>1*, taller and narrower cylindrical annular zones arise and with *A<<1* shorter and wider geometries are produced. In the former case therefore axial dimensions exceed radial dimensions and vice versa for the latter case. This parameter is therefore very important from the view point of *solar collector design*. In earlier plots we have considered only A= 2 i.e. the annulus is twice as high as it is wide, for which symmetrical axial velocity distributions were computed (e.g. fig. 4). In **figs. 16 and 17**, we observe that as *A* increases from 1 through 2, 5 to 10, both axial and radial flow are accelerated. However the parabolic distribution of axial flow (**fig. 16**) at low aspect ratio is transformed to a strong plateau distribution at large aspect ratio i.e. the profiles are evened out in the axial direction. The radial flow is not affected in this way- for *any aspect ratio* a homogenous profile is obtained across the radial gap (**fig. 17**). Magnitudes of axial velocity are however greater at higher aspect ratio than corresponding radial velocities. The constriction in geometry of the annulus with greater aspect ratio results in a slight decrease in temperature (**fig. 18**) whereas it leads to a strong elevation in radiative moment of intensity, this being sustained for all radial coordinates (**fig. 19**). Evidently geometrical configuration of the medium has a marked influence on the propagation of thermal radiation and momentum diffusion, whereas it has a weak influence on thermal diffusion. Since greater radiative moment of intensity is associated with better solar collector performance, it would appear that taller and slender solar

collectors achieve enhanced efficiency compared with shorter and wider cells. Indeed this has been noted in several experimental studies of solar cell performance, notably [51 - 53]. Finally **figs. 20-25** illustrate the effect of *optical thickness (τ_0), a* key radiative property, on thermofluid characteristics. In the vast majority of radiative-convective studies, optical thickness is assumed to be either very small (optically thin approximation) or very large (optically thick approximation). The latter results in a Rosseland-type diffusive flux model [54]. These extreme values of optical thickness are not representative of real media in solar collectors. More robust values correlating with solar cell design fall between 0.1 and 1, and these are implemented in the present computations. As optical thickness (optical depth) increases, thermal radiation is better attenuated in the medium and this induces heating. Optical thickness is a dimensionless quantification of how much a given medium retards the passage of thermal radiation. Radiative intensity falls by an exponential factor when optical thickness is unity. Physically optical thickness will be a function of absorption coefficient, medium density and propagation distance. Strong *axial flow acceleration* is generated with greater optical thickness (fig. 20) whereas *weak radial deceleration* (fig. 21) is produced. Figs. 22 and 23 show that both axial and radial temperature distributions are strongly enhanced as the medium becomes more optically thick. Higher temperatures are observed in the radial direction however. Lord and Arpaci [55] have observed a strong increase in temperatures with increasing optical thickness- this trend is confirmed in the present study. A weak decrease in radiative moment of intensity distribution with radial coordinate is caused with increasing optical thickness (fig. 24). Conversely at low and high axial coordinates, radiative moment of intensity is elevated with optical thickness whereas at intermediate axial coordinate values it is depressed. Optical thickness therefore exerts a *consistent and negative effect* in the radial direction whereas the influence is more complex

in the axial direction (fig. 25). This has important implications in optimized solar cell design.

6. CONCLUSIONS

An axisymmetric (*X, R*) dimensionless heat transfer model has been developed for the radiative-convective flow of a gray fluid in an absorbing-emitting fluid-saturating a porous medium contained in a cylindrical annulus regime, as a simulation of a hybrid solar energy collector system. The *Traugott P1-Differential radiative transfer model* has been used to analyze radiative flux and transpose the general integral radiative equation to a partial differential equation. The nonlinear Darcy-Forcheimmer porous medium drag force model is utilized with isotropic permeability (i.e. the same permeability in both the radial (*R*) and axial (*X*) directions), in order to study the effects of more complex porous absorber materials on the thermofluid dynamics. A finite difference numerical scheme has been employed to compute the velocity, temperature and radiation intensity distributions in the regime, for the effects of *conduction-radiation parameter (N), Forcheimmer parameter (Fs), Rayleigh buoyancy number (Ra), annulus aspect ratio (A), Darcy number (Da)* and *optical thickness (τ_0)*. Greater aspect ratio has been shown to generally accelerate flow and enhance radiative moment of intensity. Larger Darcy number and Forchheimer number, respectively accelerate and decelerate the axial and radial flow. With greater optical thickness of the saturated porous medium, radial flow is weakly retarded, axial flow is accelerated, temperatures are enhanced, however radial distributions of radiative moment of intensity are slightly depressed whereas at high and low axial coordinate values, radiative moment of intensity values are boosted. The current study has applications in hybrid porous media absorber solar energy systems. Although quite sophisticated

characteristics have been studied herein, the work can be refined to examine *slip flows* [56]

and furthermore *non-Newtonian* working fluids [57].

REFERENCES

[1] Khoukhi, M., Maruyama, S., Sakai, S. and Behnia, M., Combined non-gray radiative and conductive heat transfer in solar collector glass cover, *Solar Energy*, 75, 285-293 (2003).

[2] Jossen, A., Garche, J., Doering, H., Goetz, M., Knaupp, W. and Joerissen, L., Hybrid systems with lead–acid battery and proton-exchange membrane fuel cell, *J. Power Sources*, 144, 2, 395-401 (2005).

[3]Bergoug, N., Kadid, F.Z. and Abdessemed, R., Numerical modeling of the electro-magnetic model of an annular induction MHD pump by the finite volume method, *SPEEDAM 2008: Int. Symp. Power Electronics and Electrical Drives, Automation and Motion, June, Ischia, Italy* (2008).

[4] Adamiak, K., Mizuno, A., Nakano, M., Electrohydrodynamic flow in optoelectrostatic micropump: experiment versus numerical simulation, *IEEE Industry Applications Conference, 23-27 September, New Orleans, Louisiana, USA* (2007).

[5] Nascimento, M.A.R., Lora, E.S., Corrêa, P.S.P., Andrade, R.V., Rendon, M.A., Venturini, O.J. and Ramirez, G.A.S., Biodiesel fuel in diesel micro-turbine engines: Modelling and experimental evaluation, *Energy*, 33,2, 233-240 (2008).

[6] P. Rana, R. Bhargava and O. Anwar Bég, Finite element modelling of conjugate mixed convection flow of Al_2O_3-water nanofluid from an inclined slender hollow cylinder, *Physica Scripta,* 88, 1-15 (2013).

[7] Alvarez, G. and Estrada, C. A., Numerical heat transfer in a cavity with a solar control coating deposited to a vertical semitransparent wall, *Int. J. Numerical Methods Fluids*, 34, 7, 585-607 (2000).

[8] O. Anwar Bég, M. Hameed and T.A. Bég, Chebyschev spectral collocation simulation of nonlinear boundary value problems in electrohydrodynamics, *Int. J. Computational Methods Engineering Science Mechanics,* 14, 104-115 (2013).

[9] J. Vandamme, Q. Zou, D. Reeve and Y. Zhang, Modelling the movement and wave impact of a floating object using SPH, *Proc. 8th European Wave and Tidal Energy Conference, Uppsala, Sweden* (2009).

[10] M.M. Rashidi, O. Anwar Bég, A. Basiri Parsa, F. Nazari, Analysis and optimization of a transcritical power cycle with regenerator using artificial neural networks and genetic algorithms, *Proc. IMechE. Part A: J. Power and Energy*, 225, 701-717 (2012).

[11] C. N. P. Sze, B. R. Hughes and O. Anwar Bég, Computational study of improving the efficiency of photovoltaic panels in the UAE, *ICFDT 2011-International Conference on Fluid Dynamics and Thermodynamics, Dubai, United Arab Emirates, January 25-27,* (2011).

[12] S.K. Ghosh, O. Anwar Bég, J. Zueco and Prasad, V. R., Transient hydromagnetic flow in a rotating channel permeated by an inclined magnetic field with magnetic induction and Maxwell displacement current effects, *ZAMP: J. Applied Mathematics and Physics*, 61, 147-169 (2010).

[13] O. Anwar Bég, M.M. Rashidi, M. Akbari, A. Hosseini, Comparative numerical study of single-phase and two-phase models for bio-nanofluid transport phenomena, *J. Mechanics in Medicine and Biology* 14, 1450011 (2014) (31 pages).

[14] Hottel, H.C. and Sarofim, A.F., *Radiative Transfer*, McGraw-Hill, New York (1967).

[15] D.L. Siebers and R. Viskanta, Thermal analysis of some flat-plate solar collector designs for improving performance, *AIAA J. Energy*, 3, 1, 8-15 (1979).

[16] Bohn, Mark S. and Mehos, Mark S., Radiative transport models for solar thermal receiver/reactors, *ASME Int. Solar Energy Conference, Miami, Florida, 1-4 April* (1990).

[17] Chow, T.T. and A. L. S. Chan, Numerical study of desirable solar-collector orientations for the coastal region of South China, *Applied Energy*, 79, 249-260 (2004).

[18] Ralf Leutz; Hans Philipp Annen, Energy performance modelling of stationary and quasi-stationary solar concentrators based on reverse ray-tracing, *IEEE 4th World Conference on Photovoltaic Energy Conversion, May, 714-717, Hawaii, USA* (2006).

[19] Augustus, L.M. and Kumar, S., Mathematical modeling and thermal performance analysis of unglazed transpired solar collectors, *Solar Energy*, 81, 62-75 (2007).

[20] P. Naphon, Effect of porous media on the performance of the double-pass flat plate solar air heater, *Int. Comm. Heat Mass Transfer*, 32, 140-150 (2005).

[21] K. Sopian, M.A. Alghoul, E.M. Alfegi, M.Y. Sulaiman, and E.A. Musa, Evaluation of thermal efficiency of double-pass solar collector with porous-nonporous media, *Renewable Energy*, 34, 640-645 (2009).

[22] Kleinstreuer, C. and H. Chiang, Analysis of a porous-medium solar collector, *Heat Transfer Engineering*, 11, 45 - 55 (1990).

[23] Bég, O. Anwar, H.S. Takhar, V.M. Soundalgekar and Prasad, V., Thermoconvective flow in a saturated, isotropic, homogeneous porous medium using Brinkman's model: numerical study, *Int. J. Numerical Methods Heat Fluid Flow*, 8, 559-589 (1998).

[24] Rabadi, N. J. and Mismar, S.A., Enhancing solar energy collection by using curved flow technology coupled with flow in porous media: an experimental study, *Solar Energy*, 75, 261-268 (2003).

[25] Nield, D.A and Bejan, A., *Convection in Porous Media*, Springer Verlag, New York (1992).

[26] Takhar, H.S., Bég, O. Anwar and Kumari, M., Computational analysis of coupled radiation convection dissipative flow in non-Darcy porous medium using the Keller-Box implicit difference scheme, *Int. J. Energy Research*, 22,141-159 (1998).
[27] Nagaraju, P., Chamkha, A.J., Takhar, H.S. and Chandrasekhara. B.C.: Simultaneous radiative and convective heat transfer in a variable porosity medium, *Heat and Mass Transfer,* 37, 243-250 (2001).

[28] Bég, O. Anwar and Takhar, H.S., Mathematical Modeling of dissipative Darcy-Forcheimmer flow of convective-radiative viscoelastic flow in non-Darcy porous medium using the Rossleand radiative transfer model, *5th World Congress on Computational Mechanics, Vienna University of Technology, Wein, Vienna, Austria, July* (2002).

[29] Bég, O. Anwar, H. S. Takhar, A. J. Chamkha, D. Filip and I. Pop, Mixed radiation-convection flow of an optically dense viscous fluid along a vertical surface in a non-Darcy porous medium, *Int. J. Applied Mechanics and Engineering*, 8, 483-496 (2003).

[30] Bég, O. Anwar, J. Zueco, Bég, T. A., H. S. Takhar and E. Kahya NSM analysis of time-dependent nonlinear buoyancy-driven double-diffusive radiative convection flow in non-Darcy geological porous media, *Acta Mechanica*, 202, 181-204 (2009).

[31] Bég, O. Anwar, J. Zueco, H.S. Takhar, T.A. Bég, A. Sajid, Transient nonlinear optically-thick radiative–convective double-diffusive boundary layers in a Darcian porous medium adjacent to an impulsively started surface: Network simulation solutions *Comm. Nonlinear Science and Numerical Simulation*, 14, 3856-3866 (2009).

[32] Bouallou, C. and Sacadura, J.F., Thermal radiation, conduction and convection in porous media constrained in 2-D vertical enclosures, *ASME J. Heat Transfer*, 113, 255-258 (1991).

[33] Traugott, C., Radiative heat-flux potential for a non-gray gas, *AIAA J.*, 4, 541-542 (1966).

[34] Bayazitoglu, Y. and Higenyi, J., High-order differential equation of radiative transfer: P3 Approximation, *AIAA J.*, 17, 424-431 (1979).

[35] Bég, O. Anwar, Zueco, J and Lopez-Ochoa, L. M., Network numerical analysis of optically thick hydromagnetic slip flow from a porous spinning disk with radiation flux, variable thermophysical properties, and surface injection effects, *Chemical Engineering Communications*, 198, 360-384 (2011).

[36] D. Gupta, L. Kumar, O. Anwar Bég and B. Singh, Finite element simulation of mixed convection flow of micropolar fluid over a shrinking sheet with thermal radiation, *Proc IMechE- Part E: J. Process Mechanical Engineering*, 228, 61-72 (2014).

[37] Weng, L.C. and Chu, H.S., Combined natural convection and radiation in a vertical annulus, *Heat and Mass Transfer*, 31, 371-379 (1996).

[38] K. A. Hoffmann, S. T. Chiang, *Computational Fluid Dynamics*, Engineering Edition System, Wichita, Kansas, USA (2000).
[39] N. Ali, A. Zaman and O. Anwar Bég, Numerical simulation of unsteady micropolar hemodynamics in a tapered catheterized artery with a combination of stenosis and aneurysm, *Medical Engineering and Physics* (2015).*Under review*

[40] A. Zaman, N. Ali and O. Anwar Bég, Unsteady magnetohydrodynamic blood flow in a porous-saturated overlapping stenotic artery: Numerical modelling, *J. Mechanics in Medicine and Biology* (2015).

[41] N. Ali, K. Javid, M. Sajid and O. Anwar Bég, Numerical simulation of peristaltic flow of a biorheological fluid with shear-dependent viscosity in a curved channel, *Computer Methods in Biomechanics and Biomedical Engineering* (2015).

[42] L. W. Nagel, SPICE2: A computer program to simulate semiconductor circuits, *Electronics Research Laboratory Report #ERL-M520, University of California, Berkeley, USA, May* (1975).

[43] J. Zueco and O. Anwar Bég, Network numerical analysis of hydromagnetic squeeze film flow dynamics between two parallel rotating disks with induced magnetic field effects, *Tribology International*, 43, 532-543 (2010).

[44] O. Anwar Bég, J. Zueco, M. Norouzi, M. Davoodi, A. A. Joneidi, Assma F. Elsayed, Network and Nakamura tridiagonal computational simulation of electrically-conducting biopolymer micro-morphic transport phenomena, *Comp. Biol.Medicine,* 44, 44–56 (2014).

[45] O. Anwar Bég and T. A. Bég, Network and finite element simulation of electro-rheological smart dampers for seismic applications, *Technical Report GEO-ELECTRO-4/13, 65pp Gort Engineering, Bradford and Manchester, UK, July* (2013).

[46] O. Anwar Bég and T. A. Bég, Network electrothermal model for electro-kinetic stabilization of geotechnical embankments under severe weather, *Technical Report GEO-ELECTRO-2/13, 58pp Gort Engineering, Bradford and Manchester, UK, March* (2013).

[47] J. Zueco, O. Anwar Bég and T-B Chang, Network numerical simulation of two-dimensional nonlinear micropolar hydrodynamics in a Darcian porous medium, *Korean J. Chemical Engineering*, 26, 5, 1226-1234(2009).

[48] Zueco, J., O. Anwar Bég and Tasveer A. Bég, Numerical solutions for unsteady rotating high-porosity medium channel Couette hydrodynamics, *Physica Scripta*, 80, 1-8 (2009).

[49] O. Anwar Bég, J. Zueco and H.S. Takhar, Laminar free convection from a continuously moving vertical surface in a thermally-stratified, non-Darcian high-porosity medium: Network numerical study, *Int. Comm. Heat Mass Transfer*, 35, 7, 810-816 (2008).

[50] A. Dybbs and R.V. Edwards, A new look at porous media fluid mechanics- Darcy to turbulent, *Fundamentals of Transport Phenomena in Porous Media (J. Bear and M.Y. Corapcioglu- Editors),* Martinus Nijhoff, Netherlands (1984).

[51] L.J. Shah and S. Furbo, Vertical evacuated tubular-collectors utilizing solar radiation from all directions, *Applied Energy*, 78, 371–395 (2004).

[52] A. A. Badran, Thermal performance of a cylindrical solar collector, *Energy Conversion and Management*, 32, 217–222 (1991).

[53] C. Choudhury, N.K. Bansal and H.K. Sehgal, Heat loss optimisation of a concentric cylindrical solar collector employing a cobalt oxide selective absorber, *Applied Energy*, 14, 143-159 (1983).

[54] O. Anwar Bég, M. J. Uddin, M.M. Rashidi, and N. Kavyani, Double-diffusive radiative magnetic mixed convective slip flow with Biot and Richardson number effects, *J. Engineering Thermophysics,* 23 (2), 79-97 (2014).

[55] H. A. Lord and V. S. Arpaci, Effect of non-gray thermal radiation on laminar forced convection over a heated horizontal plate, *Int. J. Heat Mass Transfer*, 13, 1737-1751 (1970).

[56] O. Anwar Bég, W.A. Khan and M.J. Uddin, Multiple slip effects on unsteady magnetohydrodynamic nanofluid transport with heat generation/absorption effects in temperature dependent porous media, *J. Porous Media,* 18, 907-922 (2015).

[57] V. R. Prasad, S. A. Gaffar and O. Anwar Bég, Heat and mass transfer of a nanofluid from a horizontal cylinder to a micropolar fluid, *AIAA J. Thermophysics and Heat Transfer,* 29, 1, 127-139 (2015).

FIGURES
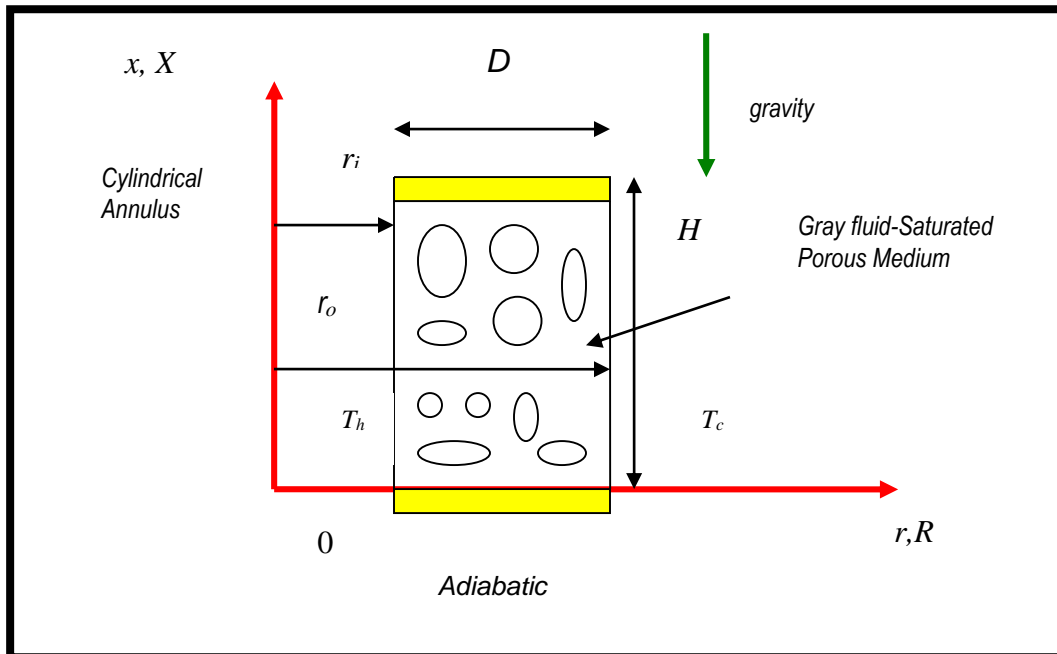
Figure 1: Radiative convection in a cylindrical isotropic porous medium annulus
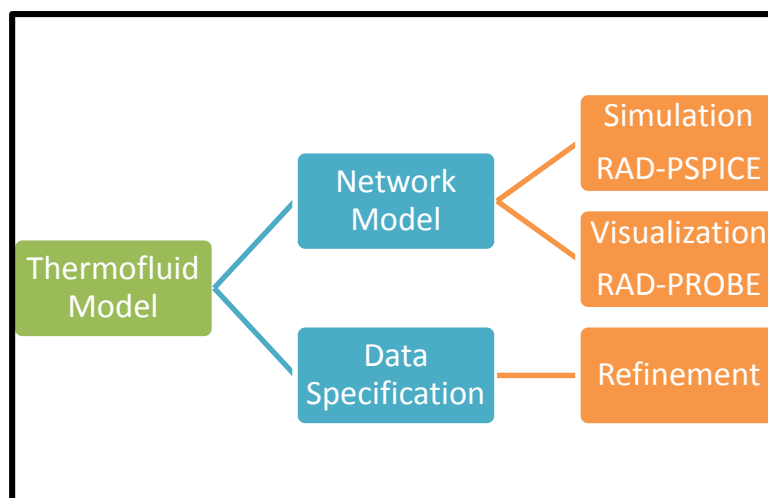
Fig. 2: RAD-PSPICE network simulation methodology
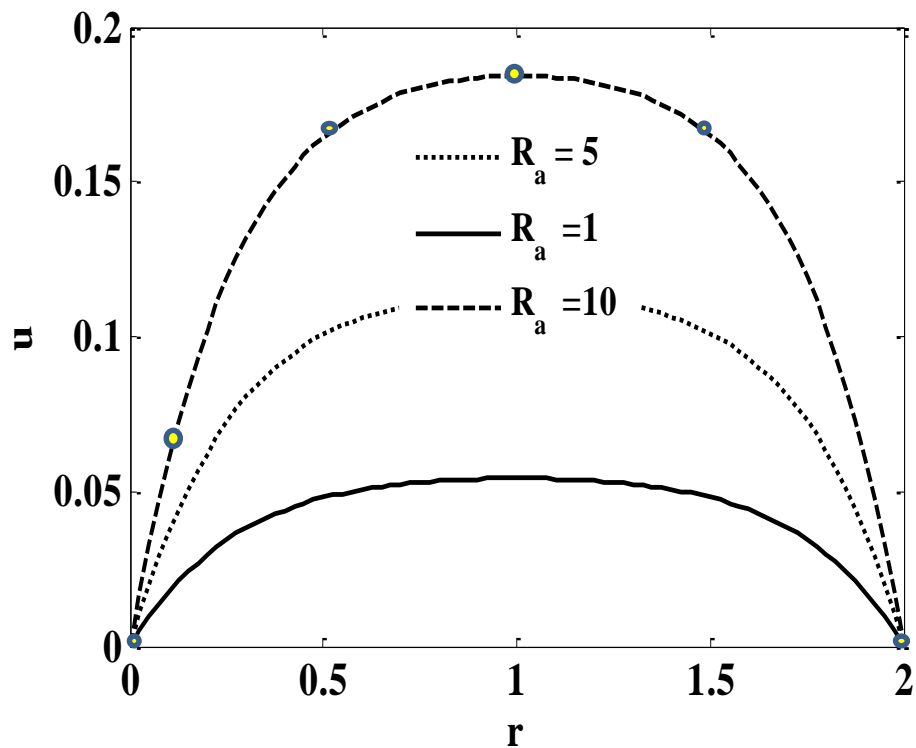
Fig 3: Axial velocity (*U*) versus radius (at *X* = 1) for *Pr* =7.0, *Da* = 0.1, *Fs* = 1, *λ* =1, *χ* =1, *τ₀* = 0.1, *Θf* =0.5, N = 1, A = 2, *rᵢ* = 0.5. [**RAD-SPICE** case validated for Rₐ =5]
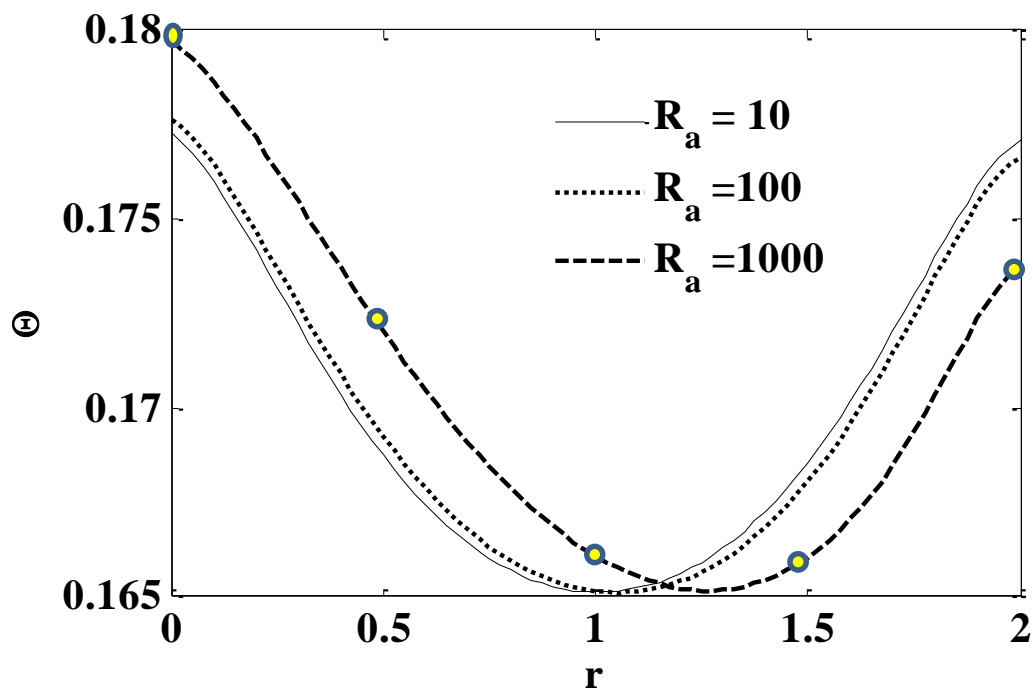
Fig 4: *Temperature (Θ) versus radius (at X = 1) for Pr = 2.0, Da = 0.1, Fs = 1, λ =1, χ =1, τ₀ = 0.1, Θf =0.5, N = 1, A = 2, rᵢ = 0.5 for various Rayleigh numbers.* [**RAD-SPICE** case validated for Rₐ =1000]
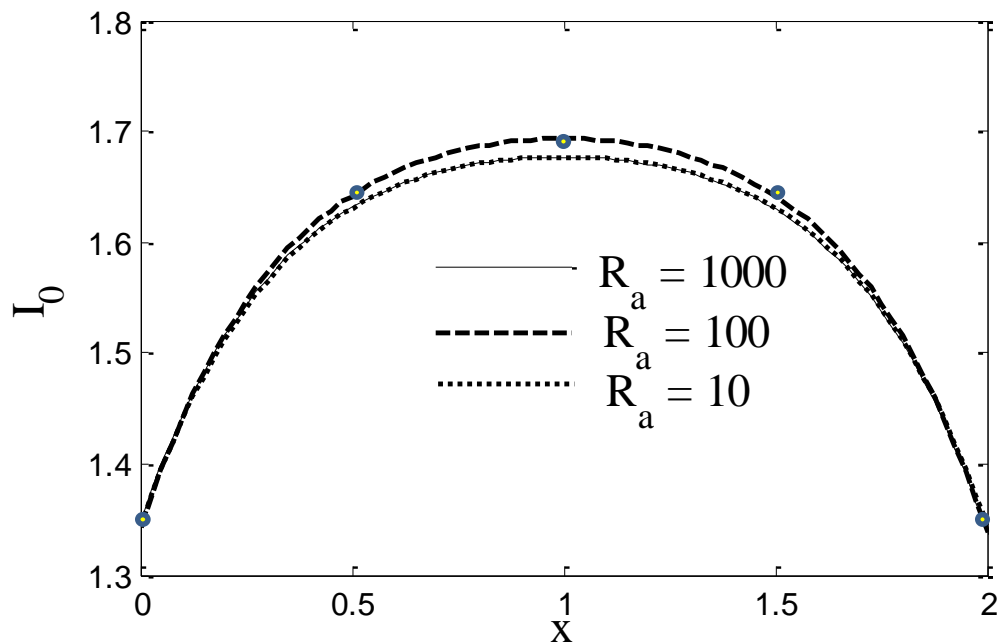
Fig 5: *Dimensionless zero moment of intensity (I_0) versus X (at R = 1) for Pr =2.0, Da = 0.1, Fs = 1, λ =1, χ =1, $τ_0$ = 0.1, $Θ_f$ =0.5, N = 1, A = 2, r_i = 0.5 for various Rayleigh numbers.* [**RAD-SPICE** case validated for R_a =100]
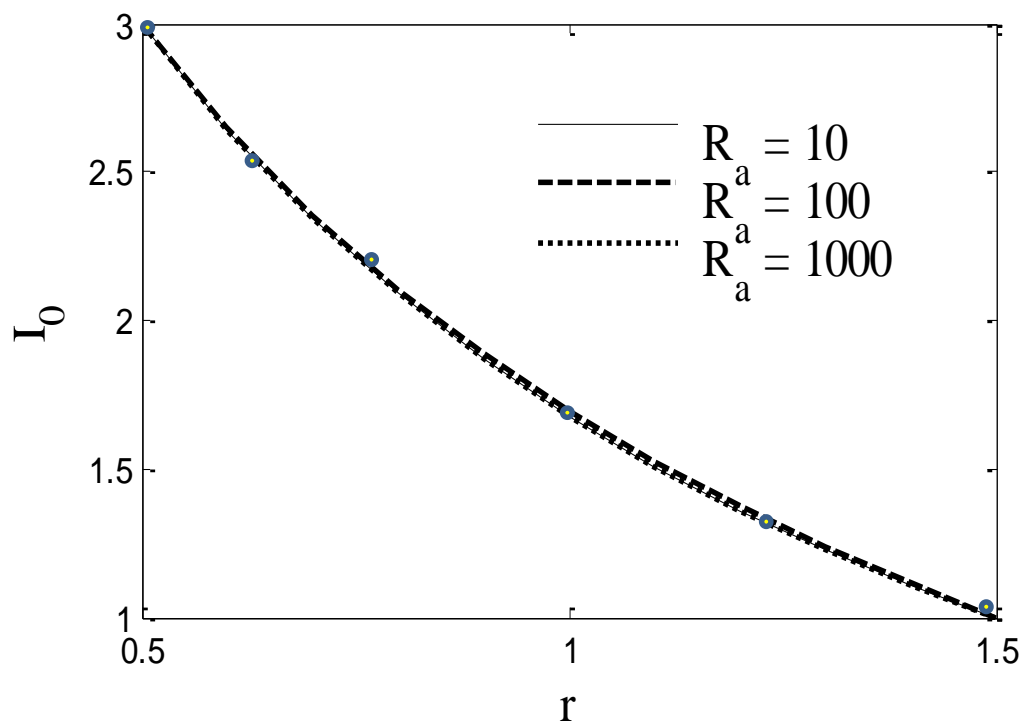
Fig. 6: *Dimensionless zero moment of intensity (I_0) versus radial coordinate (at X = 1) for Pr =2.0 (water), Da = 0.1 (high permeability), Fs = 1 (weak quadratic porous drag), λ =1, χ =1, $τ_0$ = 0.1, $Θ_f$ =0.5, N = 1, A = 2, r_i = 0.5 for various Rayleigh numbers.* [**RAD-SPICE** *validation for R_a =10*]
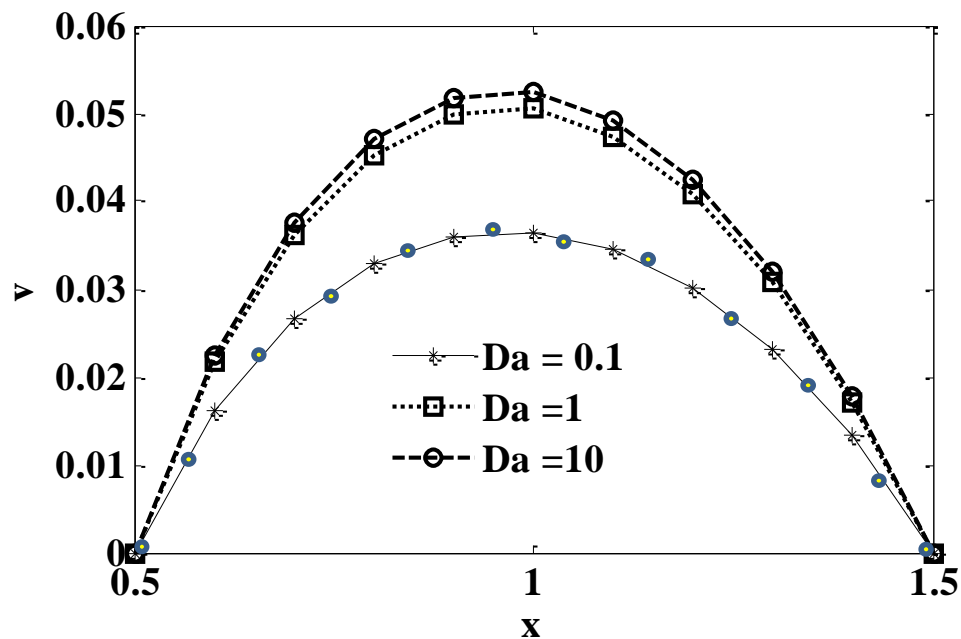
Fig. 7: *Radial velocity versus X (at R = 1) for Pr =2.0, Ra = 10, Fs = 1, λ =1, χ =1, τ_0 = 0.1, Θ_f=0.5, N = 1, A = 2, r_i = 0.5 for various Darcy numbers.* [**RAD-SPICE** validation for Da =0.1]
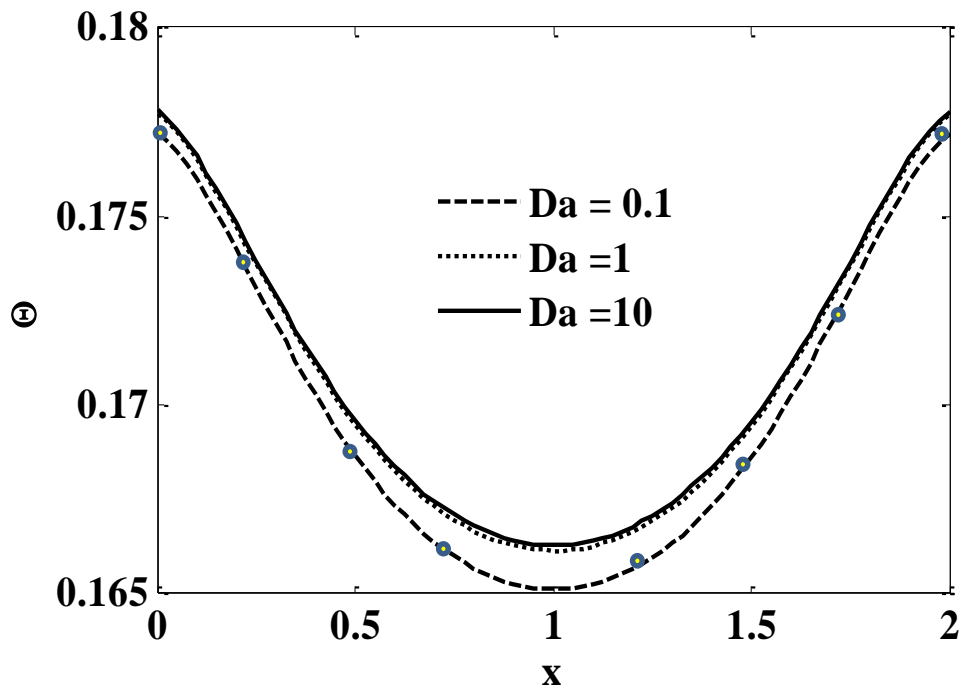
Fig. 8: *Temperature (Θ) versus axial coordinate (X) at R = 1, for Pr =2.0, Ra = 10, Fs = 1, λ =1, χ =1, τ_0 = 0.1, Θ_f=0.5, N = 1, A = 2, r_i = 0.5 for various Darcy numbers.* [**RAD-SPICE** validation for *Da*= 0.1]
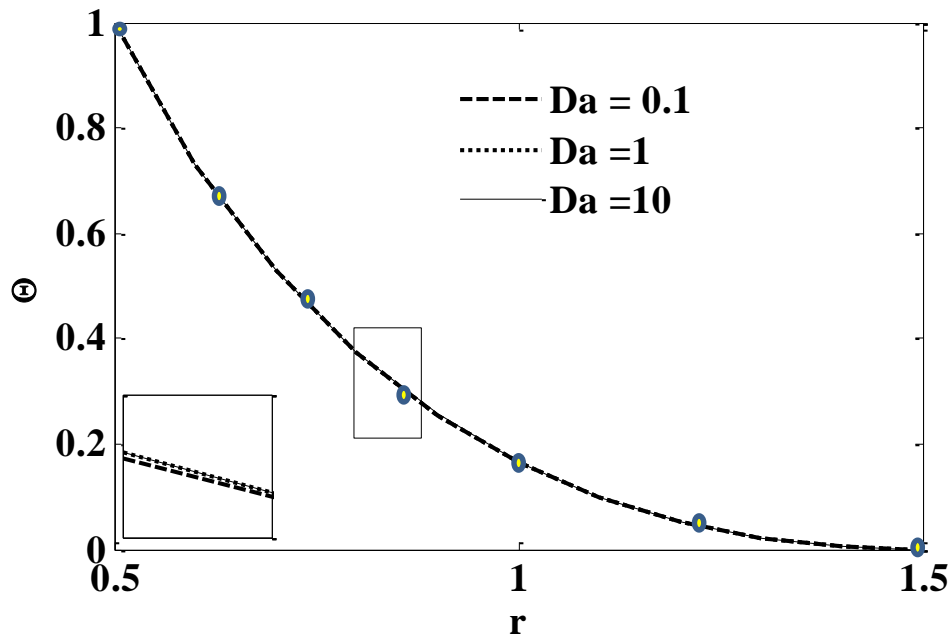
Fig. 9: *Temperature (Θ) versus radial coordinate at X = 1, for Pr =2.0, Ra = 10, Fs = 1, λ =1, χ =1, τ_0 = 0.1, Θ_f=0.5, N = 1, A = 2, r_i = 0.5 for various Darcy numbers.* [**RAD-SPICE** validation for *Da*= 1]
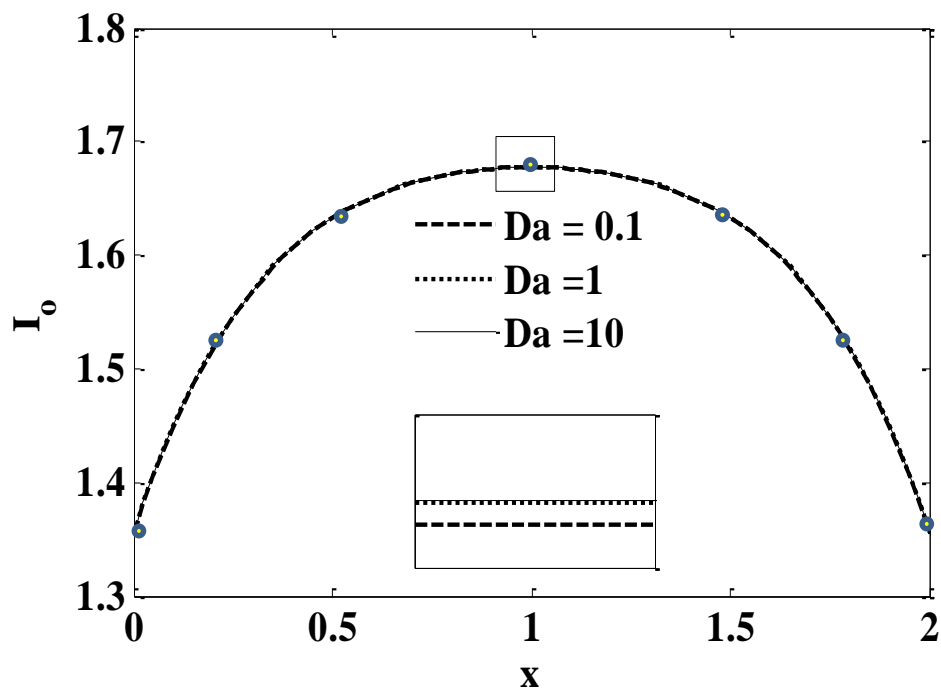
Fig. 10: *Dimensionless zero moment of intensity (I_0) versus axial coordinate (X) at R = 1, for Pr =2.0, Ra = 10, Fs = 1, λ =1, χ =1, τ_0 = 0.1, Θ_f=0.5, N = 1, A = 2, r_i = 0.5 for various Darcy numbers.* [**RAD-SPICE** validation for *Da*= 1]
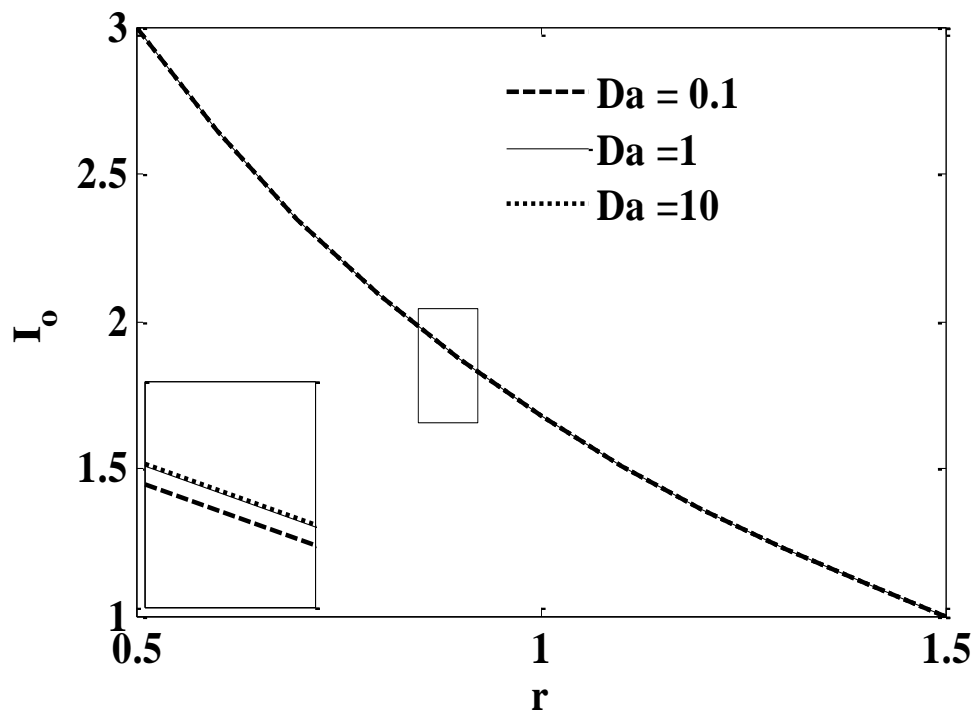
Fig. 11: *Dimensionless zero moment of intensity (I_0) versus radial coordinate at X = 1, for Pr =2.0, Ra = 10, Fs = 1, λ =1, χ =1, τ_0 = 0.1, Θ_f =0.5, N = 1, A = 2, r_i = 0.5 for various Darcy numbers.*
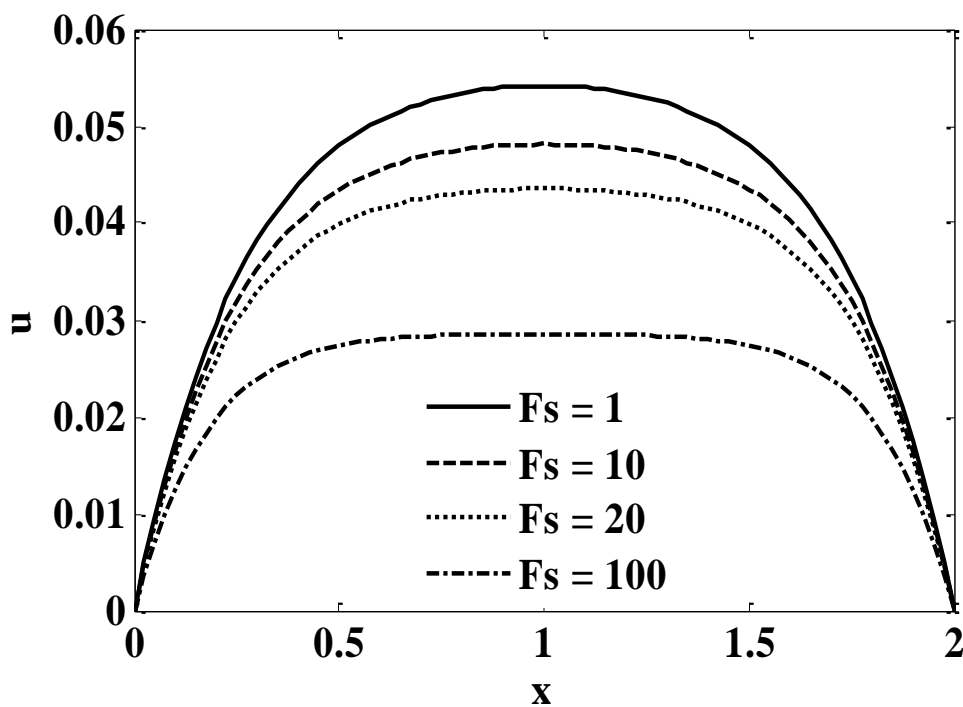
Fig. 12: *Axial velocity (U) versus X (at R = 1) with Pr =2.0, Ra = 10, Da = 0.1, λ =1, χ =1, τ_0 = 0.1, Θ_f =0.5, N = 1, A = 2, r_i = 0.5 for various Forchheimer numbers.*
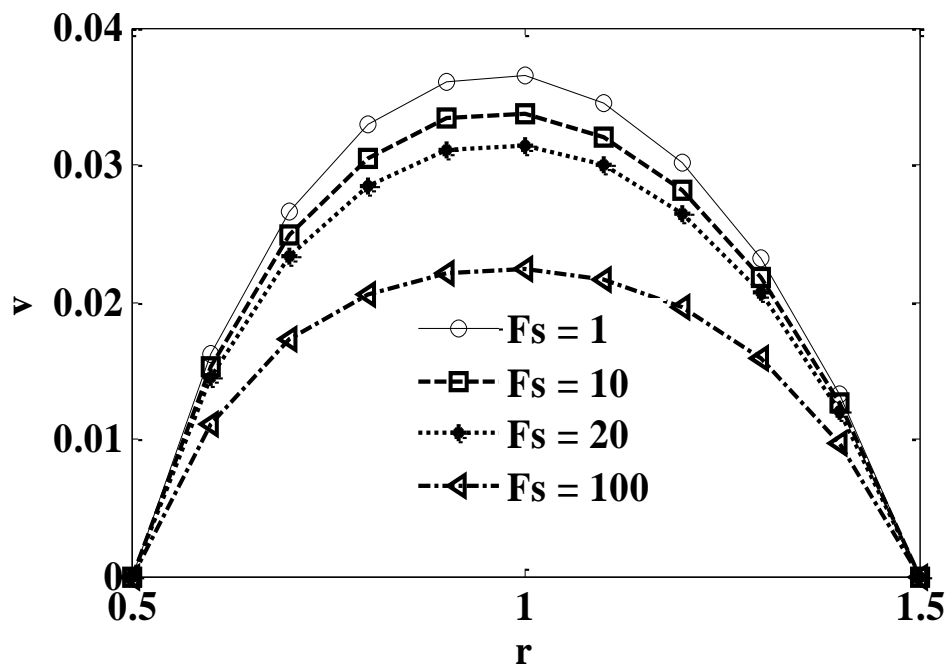
Fig. 13: *Radial velocity (V) versus radius (at X = 1) with Pr =2.0, Ra = 10, Da = 0.1, λ =1, χ =1, τ₀ = 0.1, Θf =0.5, N = 1, A = 2, rᵢ = 0.5 for various Forchheimer numbers.*
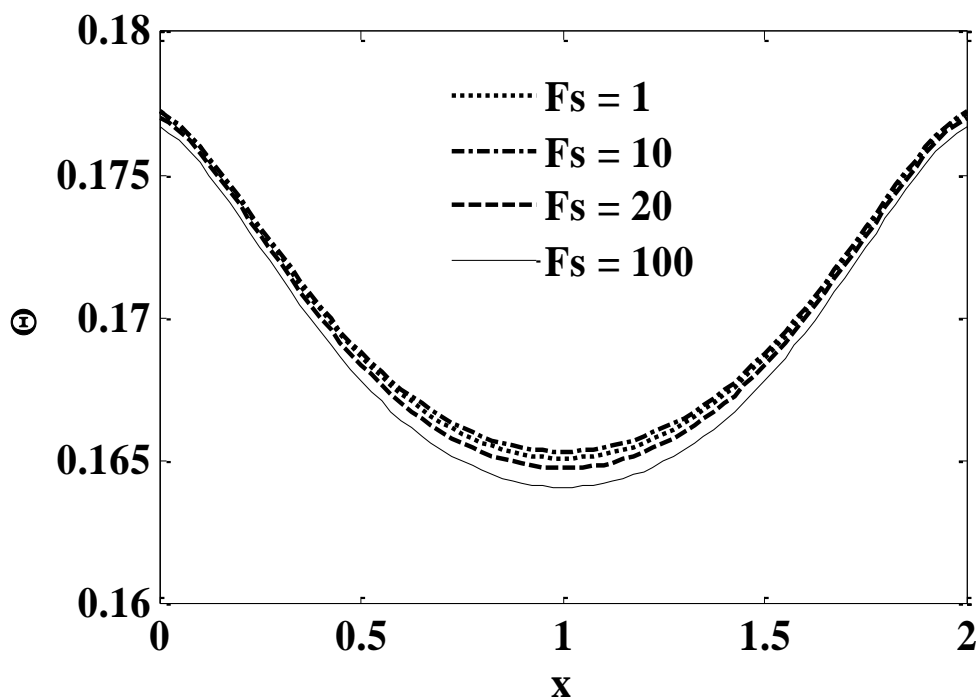
Fig. 14: *Temperature (Θ) versus axial coordinate, X, at R = 1 and Θ versus R (at X = 1) for Pr =2.0, Ra = 10, Da = 0.1, λ =1, χ =1, τ₀ = 0.1, Θf =0.5, N = 1, A = 2, rᵢ = 0.5 for various Forchheimer numbers.*
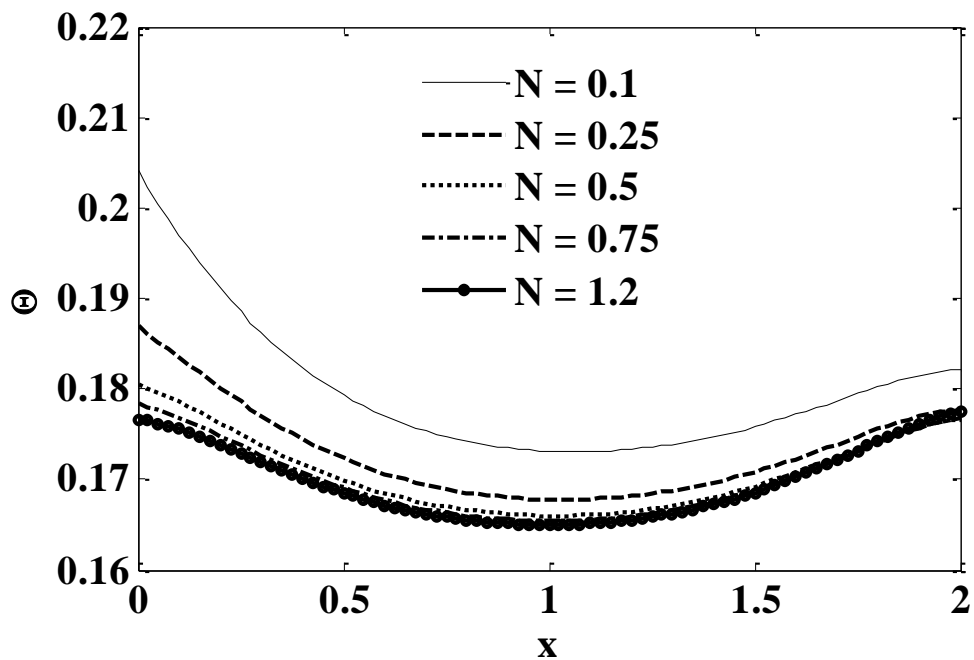
Fig. 15: *Temperature (Θ) versus axial coordinate (X) at R = 1 with Pr =2.0, Ra = 10, Da = 0.1, Fs = 1, λ =1, χ =1, τ₀ = 0.1, Θ_f =0.5, A = 2, r_i = 0.5 for various conduction-radiation parameters.*
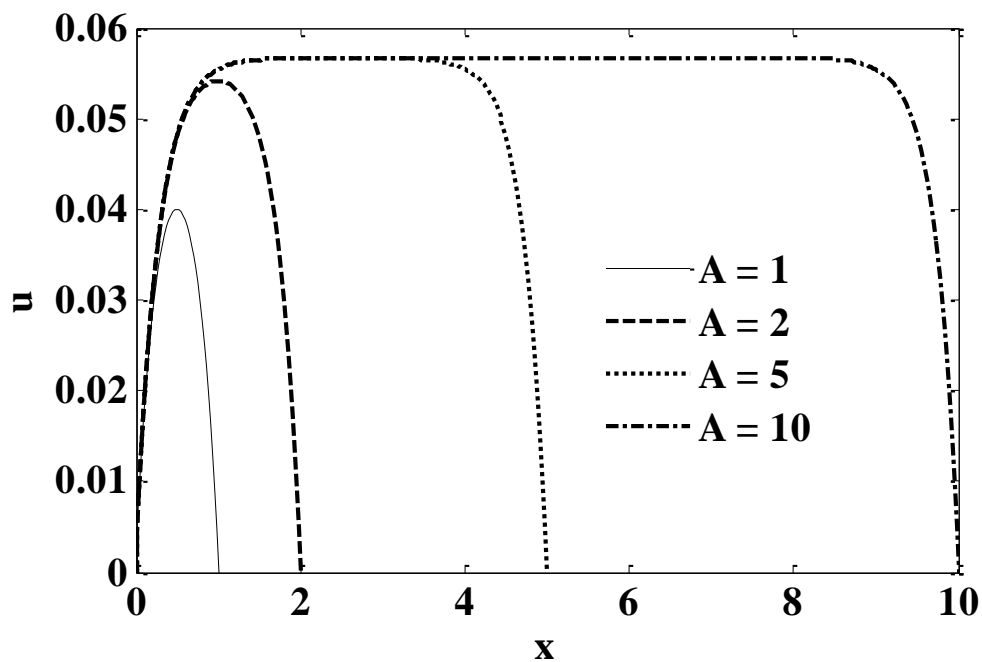
Fig. 16: *Axial velocity (U) versus axial coordinate (X), at R = 1, with Pr =2.0, Ra = 10, Da = 0.1, Fs = 1, λ =1, χ =1, τ₀ = 0.1, Θ_f =0.5, N = 1, r_i = 0.5 for various aspect ratio values.*
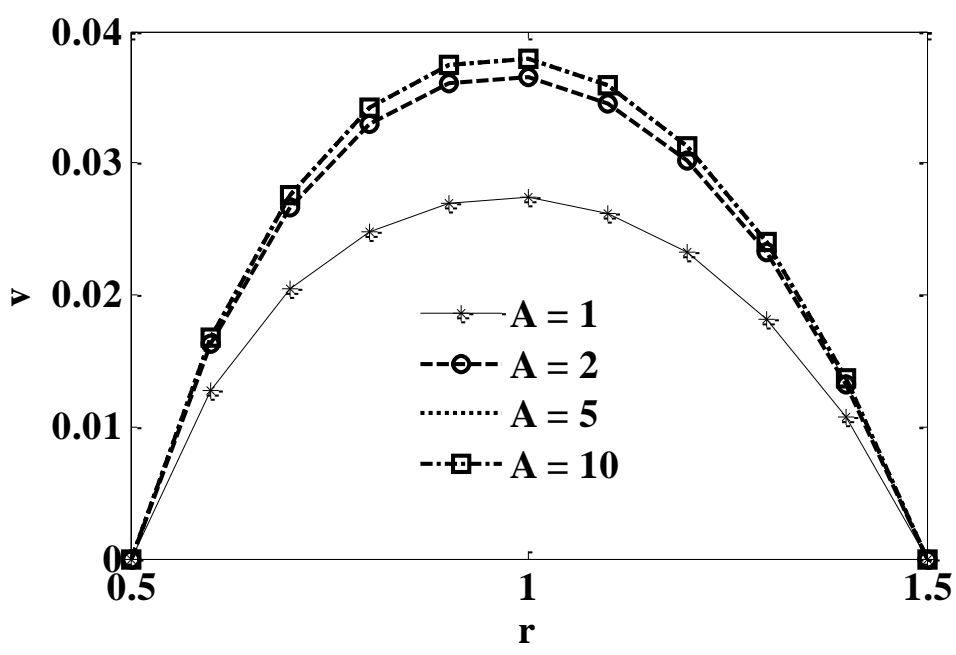
Fig. 17: *Radial velocity (V) versus radial coordinate at X = 1 with Pr =2.0, Ra = 10, Da = 0.1, Fs = 1, λ =1, χ =1, τ₀ = 0.1, Θ_f =0.5, N = 1, rᵢ = 0.5 for various aspect ratio values.*
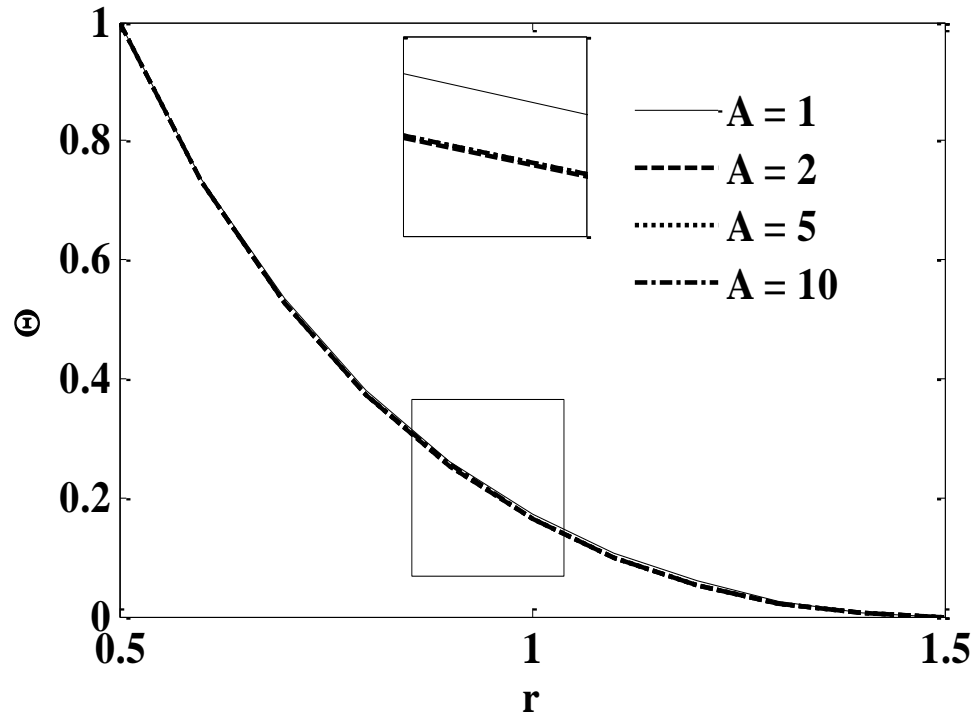
Fig. 18: *Temperature (Θ) versus radial coordinate, at X = 1, with Pr =2.0, Ra = 10, Da = 0.1, Fs = 1, λ =1, χ =1, τ₀ = 0.1, Θ_f =0.5, N = 1, rᵢ = 0.5 for various A values (1, 2, 5, 10).*
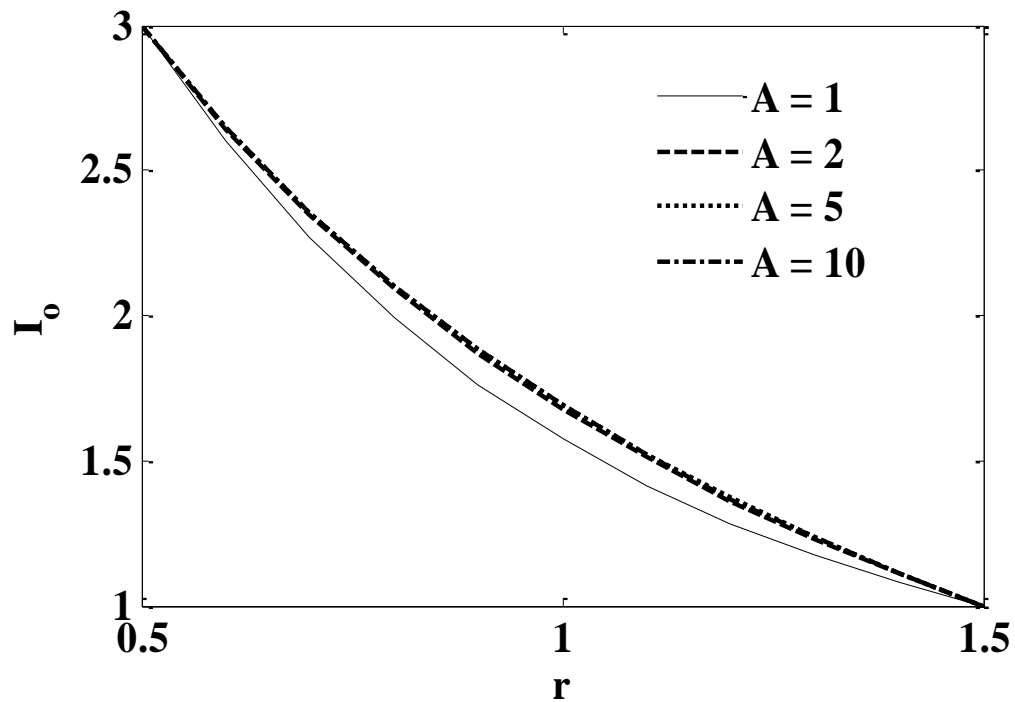
Fig. 19: *Dimensionless zero moment of intensity (I_0) versus radial coordinate at X = 1, with Pr =2.0, Ra = 10, Da = 0.1, Fs = 1, λ =1, χ =1, τ_0 = 0.1, Θ_f =0.5, N = 1, r_i = 0.5 for various aspect ratios.*
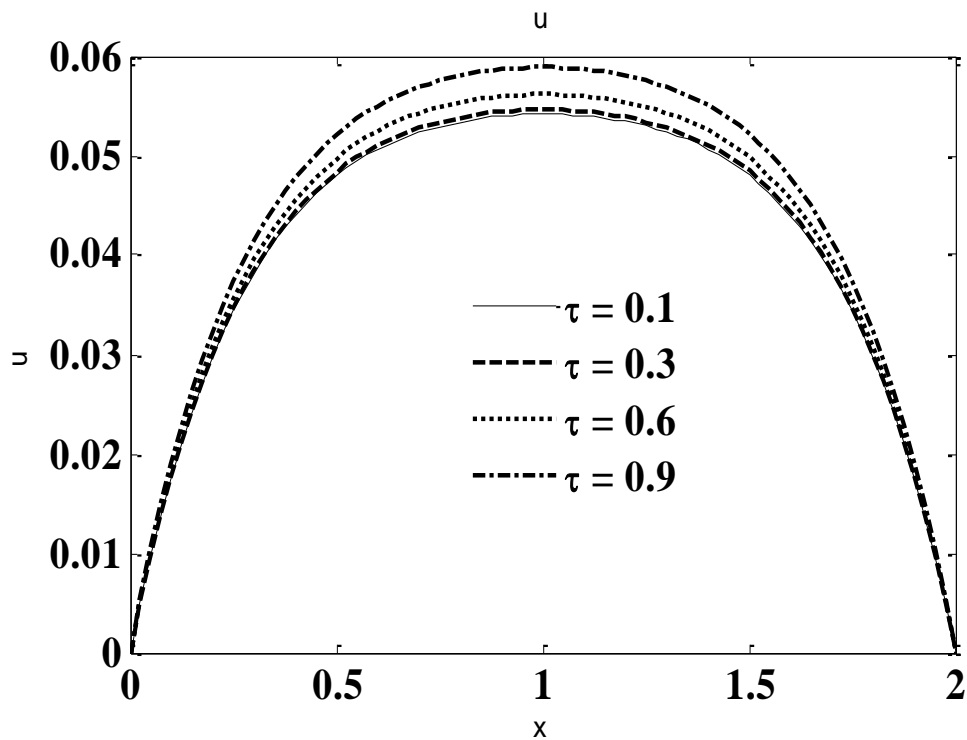
Fig. 20: *Axial velocity (U) versus X, at R = 1, with Pr =2.0, Ra = 10, Da = 0.1, Fs = 1, λ =1, χ =1, Θ_f =0.5, N = 1, r_i = 0.5, A = 2 for various optical thickness (τ_0) values.*
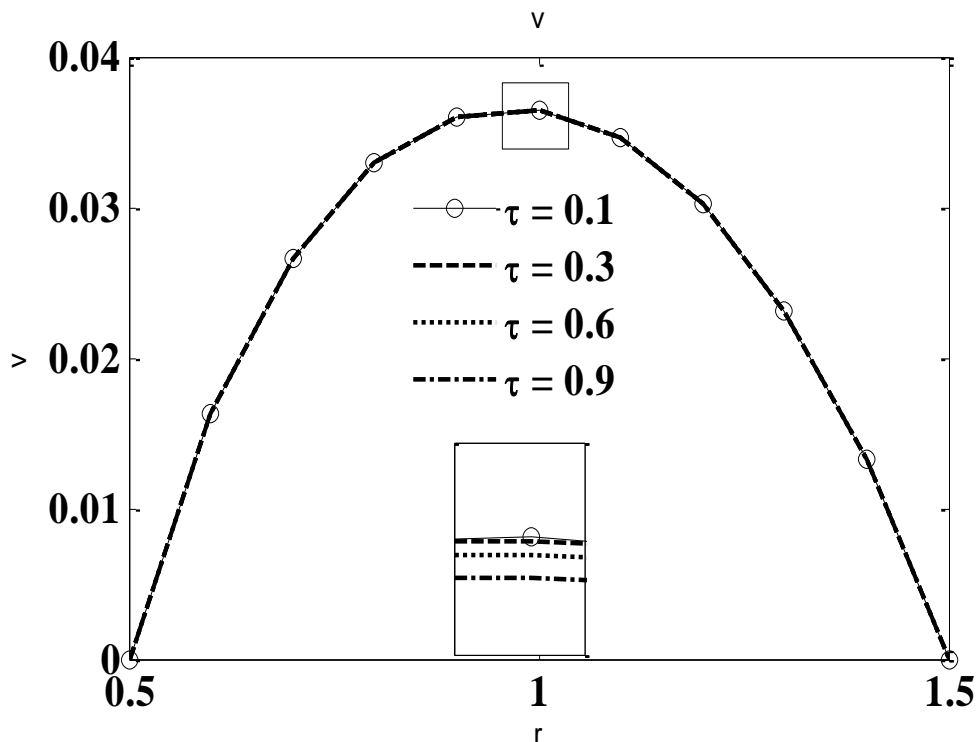
Fig. 21: *Radial velocity (V) versus radial coordinate at X = 1, with Pr =2.0, Ra = 10, Da = 0.1, Fs = 1, λ =1, χ =1, Θ$_f$ =0.5, N = 1, r$_i$ = 0.5, A = 2 for various optical thickness (τ$_0$) values.*
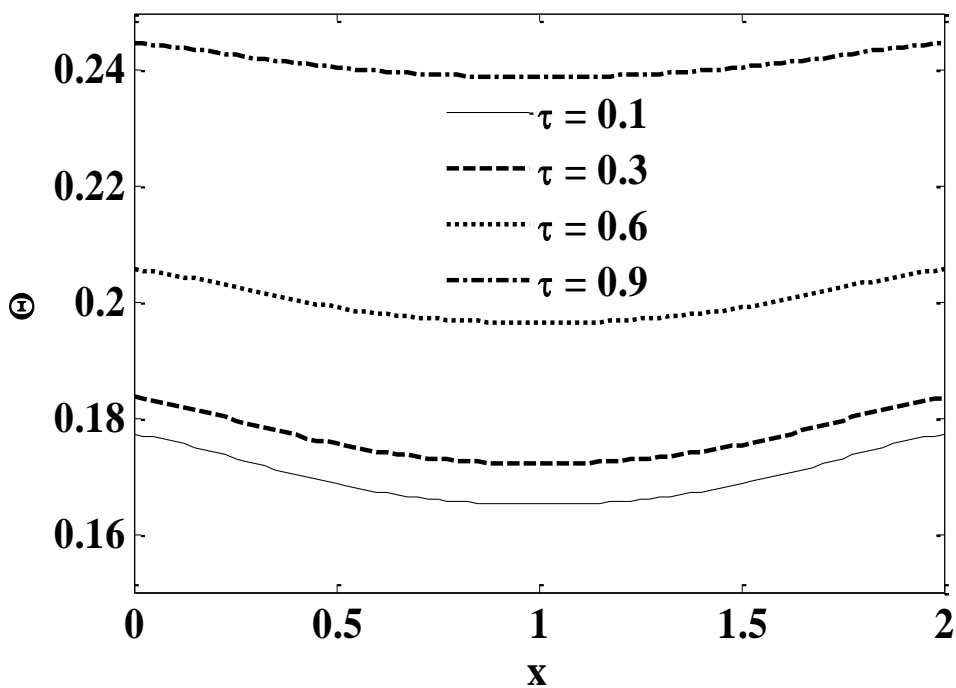
Fig. 22: *Temperature (Θ) versus axial coordinate (X) at R = 1, with Pr =2.0, Ra = 10, Da = 0.1, Fs = 1, λ =1, χ =1, Θ$_f$ =0.5, N = 1, r$_i$ = 0.5, A = 2 for various optical thickness (τ$_0$) values.*
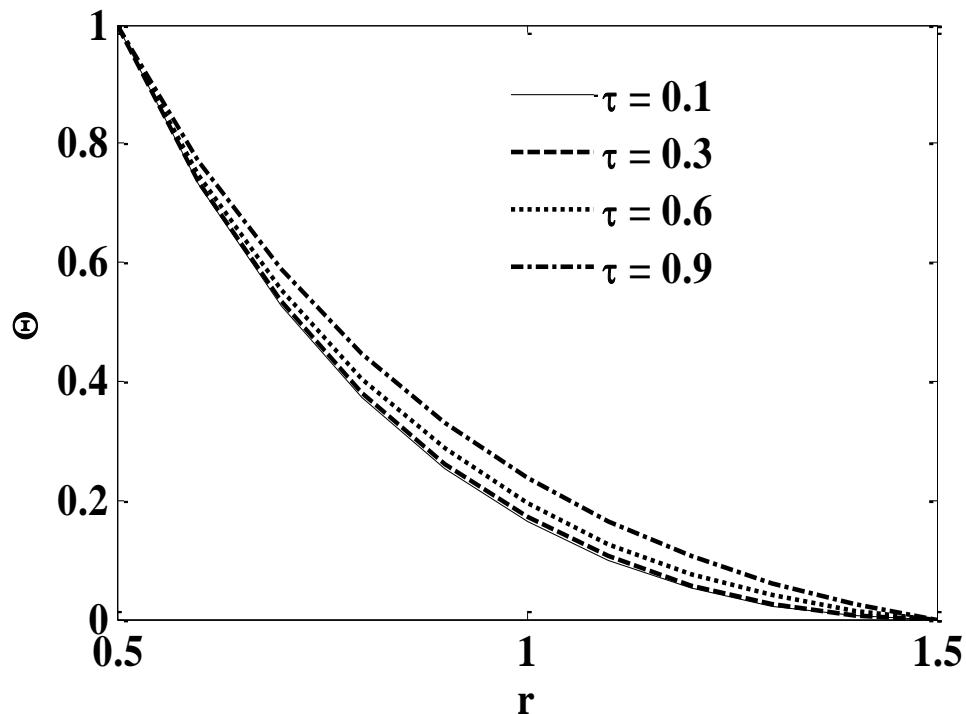
Fig. 23: *Temperature (Θ) versus radial coordinate at X = 1, with Pr =2.0, Ra = 10, Da = 0.1, Fs = 1, λ =1, χ =1, Θ_f=0.5, N = 1, r_i = 0.5, A = 2 for various optical thickness (τ_0) values.*
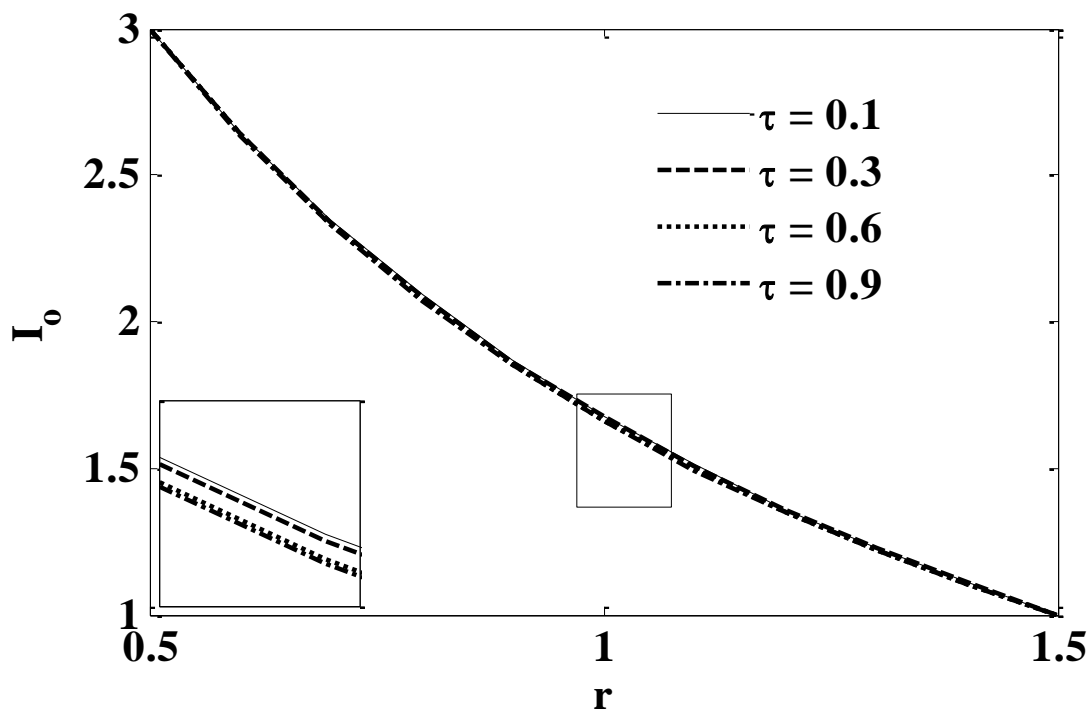
Fig. 24: *Dimensionless zero moment of intensity (I_0) versus radial coordinate at X = 1, with Pr =2.0, Ra = 10, Da = 0.1, Fs = 1, λ =1, χ =1, Θ_f=0.5, N = 1, r_i = 0.5, A = 2 for various optical thickness (τ_0) values.*

Fig. 25: *Dimensionless zero moment of intensity (I_0) versus axial coordinate (X) at R = 1 with Pr =2.0, Ra = 10, Da = 0.1, Fs = 1, λ =1, χ =1, Θ_f =0.5, N = 1, r_i = 0.5, A = 2 for various optical thickness (τ_0) values.*